



HAL
open science

A beam model for duoskelion structures derived by asymptotic homogenization and its application to axial loading problems

Emilio Barchiesi, Francesco Dell'Isola, Pierre Seppecher, Emilio Turco

► To cite this version:

Emilio Barchiesi, Francesco Dell'Isola, Pierre Seppecher, Emilio Turco. A beam model for duoskelion structures derived by asymptotic homogenization and its application to axial loading problems. European Journal of Mechanics - A/Solids, 2023, 98, pp.104848. hal-03954286

HAL Id: hal-03954286

<https://hal.science/hal-03954286v1>

Submitted on 3 May 2023

HAL is a multi-disciplinary open access archive for the deposit and dissemination of scientific research documents, whether they are published or not. The documents may come from teaching and research institutions in France or abroad, or from public or private research centers.

L'archive ouverte pluridisciplinaire **HAL**, est destinée au dépôt et à la diffusion de documents scientifiques de niveau recherche, publiés ou non, émanant des établissements d'enseignement et de recherche français ou étrangers, des laboratoires publics ou privés.

A beam model for duoskelion structures derived by asymptotic homogenization and its application to axial loading problems

Emilio Barchiesi ^{a,b}, Francesco dell’Isola ^c, Pierre Seppecher ^d, Emilio Turco ^a

^a *Università degli Studi di Sassari, Dipartimento di Architettura, design e urbanistica, Alghero, Italy*

^b *Universidad de Lima, Instituto de Investigación Científica, Santiago de Surco, Perú*

^c *Università degli Studi dell’Aquila, M&MoCS, DICEAA, L’Aquila, Italy*

^d *Université de Toulon, Institut de Mathématiques de Toulon, Toulon, France*

A B S T R A C T

Duoskelion structures have been recently introduced by Barchiesi et al. (2021) as a proof-of-concept motif for a new class of metamaterials. The properties of these periodic beam-like chiral structural elements have been investigated, up to now, by means of a discrete model formulation whose predictions are obtained by numerical methods. In this paper we select a specific scaling law for micro stiffnesses aimed at deriving, via asymptotic homogenization, an internally-constrained Cosserat one-dimensional planar continuum model as the limit of a duoskelion structure. We analyze qualitatively and quantitatively the family of equilibrium configurations of the homogenized continuum when subjected to axial loading and compare the results of the analysis with those obtained by means of the discrete model formulation.

1. Introduction

It is common experience among physicists that the behavior of mechanical discrete systems, even those consisting of simple Hooke’s springs connected with each other, can easily get very complex, even in the static regime. However, the elements of some discrete systems, while displacing in a seemingly unordered manner, show remarkable collective behaviors. Therefore, for the analysis of such systems, without even considering the computational burden that might be sometimes unbearable for extremely high degrees of freedom, a discrete model is not always the first choice. If the system is composed of a large number of similar sub-systems which appear periodically, spatially continuous formulations are able to capture the behavior of the system at large and can replace more refined discrete modeling. To pass from a discrete (micro)model to a continuum (macro)model, asymptotic homogenization techniques (Barchiesi et al., 2020; Coutris et al., 2020; dell’Isola et al., 2016), like those utilized in this paper, can be employed.

Discrete models are very often employed to deal with so-called architected materials (Turco et al., 2018, 2016; Turco, 2019; Eremeyev and Turco, 2020), in the effort of designing materials exceeding mechanical performances of conventional materials, namely exhibiting extremely favorable performances like low weight-to-stiffness ratios (Zheng et al., 2014), high element-failure tolerance (Cherkaev and Ryvkin, 2019), high energy-absorption capability (Cao et al., 2020),

customized hysteretic behavior (Vaiana et al., 2021a,b), and many others. The experimental validation of these approaches has been facilitated by the recent developments in experimental technologies, particularly referring to techniques ranging from high-resolution electron microscopy to atomic-force microscopy, which enable the examination of the material at very low scales, hence providing an unprecedented possibility to link the structure with the properties of materials (Fischer et al., 2020; Vangelatos et al., 2019a,b,c). The establishment of such a link between the (micro)structure and the observed (macro)behaviors is indeed an active area of research and is at the core of investigations in mechanical metamaterials science (Giorgio, 2016; Placidi et al., 2017; De Angelo et al., 2019).

Historically, complex architected/micro-structured media have not always attracted the interest of the community working in mechanics, especially until the second half of the nineteen-fifties. However, the significance of micro-scale mechanisms in influencing macro-scale material behaviors has been nowadays widely recognized in the context of mechanics (Abdoul-Anziz and Seppecher, 2018; Abdoul-Anziz et al., 2019, 2021; Jakabčičin and Seppecher, 2020; Yang et al., 2020, 2021, 2022) and is one of the reasons laying behind the extensive studies on second gradient and micro-polar theories (dell’Isola et al., 2012, 2017; Pietraszkiewicz and Eremeyev, 2009; Eugster et al., 2022; dell’Isola et al., 2022; Altenbach et al., 2010; Abali et al., 2015).

Indeed micro-scale mechanisms can originate interesting and characteristic macro-scale behaviors, being a complex combination of local relative displacements, buckling phenomena, folding, snapping, and many others. Many micro-structures have been investigated in the existing literature; among them, it is worth to mention those based on the pantographic motif (Seppecher et al., 2019; Turco et al., 2017; dell’Isola et al., 2019), i.e. a mechanism which is well known from everyday life (pantographic mirrors, expanding fences, scissor lifts, etc.), which is characterized by a zero-energy accordion-like uniform extension/compression deformation mode. These materials can be suitably designed to show strong anisotropic effects, namely to be extremely compliant in some directions and extremely stiff in others (Placidi et al., 2015, 2016; Eremeyev et al., 2018).

Among the many unexplored micro-structures that one could conceive, this paper is concerned with duoskelion structures, which have been recently introduced in Barchiesi et al. (2021a). Similar structures, based on a chiral geometry, have been addressed both experimentally (De Angelo et al., 2020) and theoretically (Misra et al., 2020) in the literature, but considering different connections among adjacent cells. Duoskelion structures are meant to be a proof-of-concept motif for a new class of metamaterials showing unconventional effects, like axial–transverse coupling and the co-existence of an extremely strong stiffness in compression and a relatively small stiffness in extension. Duoskelion structures have been investigated, up to now, only by means of a discrete model formulation. In this paper, we select a specific scaling of micro stiffnesses to deduce, via a formal asymptotic homogenization procedure, the deformation energy of a continuum describing the mechanical behavior of duoskelion structures. Owing to the choice of the scaling, a kinematic constraint appears at the continuum level. After having derived the continuum model, we discuss some relevant equilibrium configurations in the case of axial loads. To lighten the presentation, we will henceforth adopt the following convention: the expression *duoskelion beam* will designate the one-dimensional planar continuum obtained by homogenization, while the expression *duoskelion microstructure* will designate the discrete system.

In more details, the work is organized as follows. In Section 2, we describe the employed discrete spring (micro)model of duoskelion structures, whose elementary periodically repeated cell has size ϵ . At first, the finite-dimensional kinematics of the duoskelion microstructure is introduced. Making use of such a kinematics, the deformation energy of the duoskelion microstructure is specified. The infinite-dimensional kinematics of the target macro-scale continuum, i.e. the independent kinematic fields, is then postulated on the basis of the micro-scale kinematics. After having defined a kinematic bridging between the micro- and macro-descriptions, the asymptotic expansion of the micro-scale deformation energy, involving space derivatives of the target continuum fields evaluated at discrete points of the duoskelion microstructure, is carried out with respect to ϵ . Such an asymptotic expansion is used, together with the micro-scale stiffnesses scaling laws, to determine the ϵ -leading terms in the deformation energy. Subsequently, the quantity ϵ is let to zero — the total length of the beam-like structure is kept fixed — and the integral functional of deformation energy characterizing the continuum model is retrieved by substituting Riemann sums with integrals in space. The study being restricted to cases where the deformation energy is finite, aimed at avoiding that, for the chosen scaling law, the deformation energy blows up when ϵ tends to zero, a kinematic constraint is enforced at the macro-scale. Static condensation, namely the closed-form solution of an equilibrium equation allowing to express one kinematic field as an algebraic function of the others, is then performed on the continuum formulation to reduce the number of independent fields specifying the kinematics of the continuum.

In Section 3, equilibrium Euler–Lagrange equations associated to the continuum model are written down for the case when axial loads are considered. This is achieved by means of the introduction of an augmented Lagrangian. Subsequently, a further static condensation is

performed and reduced Euler–Lagrange equations are retrieved. Equilibrium equations are then solved in the case of uniform deformations, showing that the continuum model can behave like a mechanical diode, where the analogy (Spagnuolo and Scerrato, 2020) consists of the fact that, for a given force magnitude, negative axial displacement induced by a compression force is vanishing, while that induced by a traction force is not.

In Section 4, the Weierstrass’ qualitative study of equilibrium equations is performed by rewriting them in the form of an equivalent Hamiltonian dynamical system. The properties of such a dynamical system, inherited from its Hamiltonian structure, are not only exploited to perform a qualitative study of equilibrium solutions, but also to express them in algebraic implicit form. Linear stability analysis around the straight-beam solution for clamped-double roller boundary conditions is then performed. Results obtained in this section by means of the above-mentioned qualitative study are then used to guide the investigations carried out in the subsequent sections. Indeed, it is worth noting that, through the use of qualitative methods, the continuum formulation allows us to get a complete classification of the possible equilibrium shapes prior to any computational study. This classification will be used to guide discrete numerical simulations to get highly non-trivial equilibrium shapes.

In Section 5, some equilibrium large-deformation and large-displacement configurations are computed numerically by exploiting the implicit expression obtained in the previous section for the continuum model. Both traction and compression cases are studied.

In order to show the capabilities of the homogenized continuum model in describing the behavior of the discrete one, Section 6 presents the results, obtained by numerical simulations, of the discrete system with 50 unit cells for one of the equilibrium problems analyzed in the previous section. Finally, conclusions and outlooks are discussed.

2. Heuristic homogenization of duoskelion microstructures

In this Section, we first introduce the duoskelion micro-structure as a discrete spring model and then look for a 1D planar continuum describing synthetically its properties when the size ϵ of the periodically repeated cell is sufficiently small with respect to its total length L . To this aim, we apply a heuristic homogenization procedure, which consists in calculating the limit of the deformation energy of the discrete model for ϵ/L tending to zero. After having chosen a convenient discrete kinematics, Piola’s micro–macro identification *ansatz* is considered. It consists in introducing the kinematic macro-descriptors of the continuum as continuous functions, whose values at designated points are identified with suitable generalized coordinates of the micro-model. Exploiting such an identification, the deformation energy of the micro-model is then rewritten in terms of continuum descriptors. Taylor expansions of continuum descriptors with respect to the micro length scale ϵ are performed, aimed at expressing the deformation energy of the discrete system as a polynomial function of ϵ . Finally, the number of the periodically appearing subsystems, called cells, is increased and the stiffnesses are appropriately scaled, while the overall size of the system is kept fixed.

2.1. Discrete model

The considered family of discrete models parameterized by the cell size ϵ consists of systems of internally constrained rigid bodies interacting through extensional and rotational springs. In the undeformed configuration, see Fig. 1, a unit cell is repeated periodically along a straight line in direction of the unit basis vector $\mathbf{e}_x \in \mathbb{E}^2$. The geometry of the system presents a chiral pattern, namely it is not invariant for reflections with respect to the axes of the orthonormal basis $(\mathbf{e}_x, \mathbf{e}_y)$ in Fig. 1 and it is invariant for $\pm\pi$ rad rotations. Using the language of material symmetry groups, we can state that the geometry of the microstructure belongs to the material symmetry group Z_2 . The total

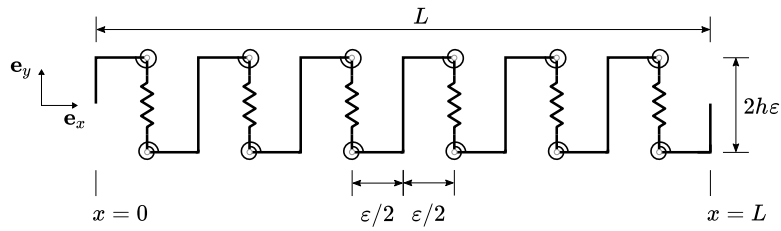


Fig. 1. Considered discrete spring model of duoskelion micro-structure. Reference geometry and graphical illustration of elastic elements and internal constraints. S-shaped bodies are rigid.

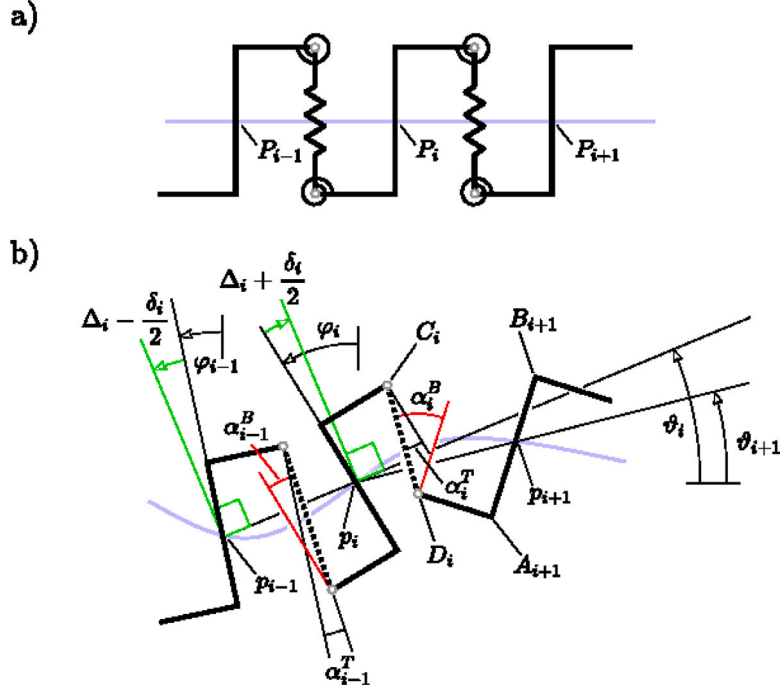


Fig. 2. Considered discrete spring model of duoskelion micro-structure. Reference and current configurations for three adjacent cells and graphical illustration of the introduced kinematic quantities.

length L of the undeformed duoskelion micro-structure encompasses $N - 1$ cells.

The cells are centered at the positions $P_i = i\epsilon\mathbf{e}_x$, for $i \in \{0, 1, \dots, N\}$, with $\epsilon = L/(N - 1)$. The height of each cell is equal to $2h\epsilon$, with h a positive constant quantity not depending on ϵ . The quantity h defines the aspect ratio of each cell. The S-shaped bodies — which are those giving the name *duoskelion* to the structure, i.e. two-legged — are rigid, while the dashed vertical links in Fig. 2 are extensional springs hinge-joined on the points C_i and D_i (see again Fig. 2) connecting two adjacent S-shaped bodies. Rotational springs are placed between extensional springs and S-shaped rigid bodies. Note that the extensional springs are rigid with respect to bending, hence they can transmit torques. White-filled circles in Fig. 1 represent hinge constraints, requiring the end points of the concurring elements to have the same position in space.

Kinematic quantities related to the discrete system and utilized throughout the paper are introduced graphically in Fig. 2. Clearly, the kinematics of the spring system is globally described by finitely many generalized coordinates. As an instance, a minimal set of coordinates for the discrete system consists of (1) the position $p_i \in \mathbb{E}^2$ of the points at position P_i in the reference configuration, and (2) the rotation angle $\varphi_i \in \mathbb{R}$ of the S-shaped rigid bodies. Aimed at simplifying formulas, and particularly to formulate the total potential energy in a most compact form, further kinematic quantities are introduced in Fig. 2, i.e. the positions $A_i, B_i, C_i, D_i \in \mathbb{E}^2$ and the angles $\Delta_i, \delta_i, \alpha_i^T, \alpha_i^B, \vartheta_i \in \mathbb{R}$. More

specifically, the quantity ϑ_i , defined for the reduced index set $i = \{1, 2, \dots, N - 2\}$, is the angle between the two vectors $p_i - p_{i-1}$ and \mathbf{e}_x .

By the definition, we have $\varphi_{i-1} = \Delta_i + \vartheta_i - \frac{\delta_i}{2}$ and $\varphi_i = \Delta_i + \vartheta_i + \frac{\delta_i}{2}$. The quantity α_i^T is the angle formed by the S-shaped rigid body centered at P_i in the reference configuration and the adjacent vertical link on the right, see Fig. 2. The quantity α_i^B is the angle formed by the S-shaped rigid body centered at P_{i+1} in the reference configuration and the adjacent vertical link on the left. The superscripts T and B stand, respectively, for *top* and *bottom*.

The micro-model deformation energy is defined as

$$\mathcal{E}_\epsilon := \sum_{i=0}^{N-1} \frac{K_{E,i}}{2} (\|C_i - D_i\| - 2h\epsilon)^2 + \frac{K_{T,i}}{2} \sin^2 \alpha_i^T + \frac{K_{B,i}}{2} \sin^2 \alpha_i^B, \quad (1)$$

with $K_{E,i} > 0$ and $K_{T,i}, K_{B,i} > 0$ being the stiffnesses of the extensional and rotational springs, respectively, and $\|\cdot\|$ being the Euclidean norm. According to Fig. 2, we have that

$$\begin{aligned} D_{i-1} - C_{i-1} &= (p_i - p_{i-1}) - \frac{\epsilon}{2} \left(\mathbf{R}_{\Delta_i + \vartheta_i - \delta_i/2} + \mathbf{R}_{\Delta_i + \vartheta_i + \delta_i/2} \right) \mathbf{e}_x \\ &\quad - h\epsilon \left(\mathbf{R}_{\Delta_i + \vartheta_i - \delta_i/2} + \mathbf{R}_{\Delta_i + \vartheta_i + \delta_i/2} \right) \mathbf{e}_y, \end{aligned} \quad (2)$$

where $\mathbf{R}_\beta : \mathbb{R}^2 \rightarrow \mathbb{R}^2$ is a linear transformation belonging to $Orth^+$ which rotates its argument by an angle β in the anti-clockwise direction, in the plane spanned by \mathbf{e}_x and \mathbf{e}_y . In matrix form, we can

write the vector $\mathbf{R}_{-\theta_i}(D_{i-1} - C_{i-1})$ in the basis $(\mathbf{e}_x, \mathbf{e}_y)$ as

$$\left[\mathbf{R}_{-\theta_i}(D_{i-1} - C_{i-1}) \right]_{(\mathbf{e}_x, \mathbf{e}_y)} = \varepsilon \begin{pmatrix} \rho_i - \cos \Delta_i \cos(\delta_i/2) + 2h \sin \Delta_i \cos(\delta_i/2) \\ -\sin \Delta_i \cos(\delta_i/2) - 2h \cos \Delta_i \cos(\delta_i/2) \end{pmatrix}, \quad (3)$$

where the quantity ρ_i has been defined as $\rho_i := \|p_i - p_{i-1}\|/\varepsilon$. Let us now consider the local, i.e. depending on the considered i th cell, orthonormal basis made up of the vectors $\mathbf{e}_{\theta_i+\Delta_i} := \mathbf{R}_{\Delta_i} \mathbf{e}_{\theta_i}$ and $\mathbf{e}_{\theta_i+\Delta_i}^\perp := \mathbf{R}_{\Delta_i} \mathbf{e}_{\theta_i}^\perp$, which is obtained by rotating in the anti-clockwise direction the local basis $(\mathbf{e}_{\theta_i}, \mathbf{e}_{\theta_i}^\perp)$ of an angle Δ_i . Noting that the equality $\left[\mathbf{R}_{-\theta_i}(D_{i-1} - C_{i-1}) \right]_{(\mathbf{e}_x, \mathbf{e}_y)} = [D_{i-1} - C_{i-1}]_{(\mathbf{e}_{\theta_i}, \mathbf{e}_{\theta_i}^\perp)}$ holds true, combining Eq. (3) and the definition of the orthonormal basis $(\mathbf{e}_{\theta_i+\Delta_i}, \mathbf{e}_{\theta_i+\Delta_i}^\perp)$ leads to

$$D_{i-1} - C_{i-1} = \varepsilon \left\{ \left[\rho_i \cos \Delta_i - \cos \left(\frac{\delta_i}{2} \right) \right] \mathbf{e}_{\theta_i+\Delta_i} - \left[\rho_i \sin \Delta_i + 2h \cos \left(\frac{\delta_i}{2} \right) \right] \mathbf{e}_{\theta_i+\Delta_i}^\perp \right\}, \quad (4)$$

that, defining the quantity $R_i := \rho_i \cos \Delta_i$, can be rewritten as

$$D_{i-1} - C_{i-1} = \varepsilon \left\{ \left[R_i - \cos \left(\frac{\delta_i}{2} \right) \right] \mathbf{e}_{\theta_i+\Delta_i} - \left[R_i \tan \Delta_i + 2h \cos \left(\frac{\delta_i}{2} \right) \right] \mathbf{e}_{\theta_i+\Delta_i}^\perp \right\}. \quad (5)$$

The last relation implies that the Euclidean norm of vector $D_{i-1} - C_{i-1}$ can be written as

$$\|D_{i-1} - C_{i-1}\|^2 = \varepsilon^2 \left\{ \left[R_i - \cos \left(\frac{\delta_i}{2} \right) \right]^2 + \left[R_i \tan \Delta_i + 2h \cos \left(\frac{\delta_i}{2} \right) \right]^2 \right\}. \quad (6)$$

We now define the unit vector $\mathbf{d}_i := \frac{B_{i-1} - p_{i-1}}{\|B_{i-1} - p_{i-1}\|}$, which lies on the line joining B_{i-1} and p_{i-1} and points toward B_{i-1} . It is straightforward to see that the vector \mathbf{d}_i can be written in the basis $(\mathbf{e}_{\theta_i}, \mathbf{e}_{\theta_i}^\perp)$ as

$$\mathbf{d}_i = -\sin \left(\Delta_i - \frac{\delta_i}{2} \right) \mathbf{e}_{\theta_i} + \cos \left(\Delta_i - \frac{\delta_i}{2} \right) \mathbf{e}_{\theta_i}^\perp \quad (7)$$

or, equivalently, in the basis $(\mathbf{e}_{\theta_i+\Delta_i}, \mathbf{e}_{\theta_i+\Delta_i}^\perp)$, as

$$\mathbf{d}_i = \sin \left(\frac{\delta_i}{2} \right) \mathbf{e}_{\theta_i+\Delta_i} + \cos \left(\frac{\delta_i}{2} \right) \mathbf{e}_{\theta_i+\Delta_i}^\perp. \quad (8)$$

Let us now consider the unit vector $\mathbf{E}_i := \frac{B_i - p_i}{\|B_i - p_i\|}$, which lies on the line joining B_i and p_i and points toward B_i . It is again straightforward to see that the vector \mathbf{E}_i can be written in the basis $(\mathbf{e}_{\theta_i}, \mathbf{e}_{\theta_i}^\perp)$ as

$$\mathbf{E}_i = \left[-\sin \Delta_i \cos \left(\frac{\delta_i}{2} \right) - \cos \Delta_i \sin \left(\frac{\delta_i}{2} \right) \right] \mathbf{e}_{\theta_i} + \left[\cos \Delta_i \cos \left(\frac{\delta_i}{2} \right) - \sin \Delta_i \sin \left(\frac{\delta_i}{2} \right) \right] \mathbf{e}_{\theta_i}^\perp \quad (9)$$

or, equivalently, in the basis $(\mathbf{e}_{\theta_i+\Delta_i}, \mathbf{e}_{\theta_i+\Delta_i}^\perp)$, as

$$\mathbf{E}_i = -\sin \left(\frac{\delta_i}{2} \right) \mathbf{e}_{\theta_i+\Delta_i} + \cos \left(\frac{\delta_i}{2} \right) \mathbf{e}_{\theta_i+\Delta_i}^\perp. \quad (10)$$

Note that, since $\Delta_{i+1} - \frac{\delta_{i+1}}{2} + \theta_i = \Delta_i + \frac{\delta_i}{2}$, one has $\mathbf{E}_i = \mathbf{d}_{i+1}$.

In conclusion, for the angle α_{i-1}^T appearing in Eq. (1), one can write as in Eqs. (11)–(13) (see Box 1), where (11) has been obtained by noting that α_{i-1}^T is the angle formed by the vectors \mathbf{d}_i^\perp and $D_{i-1} - C_{i-1}$, while (12) has been obtained by substituting Eqs. (5) and (8) in (11). Analogously, for the angle α_{i-1}^B appearing in Eq. (1), one can write as in Eqs. (14)–(16) given in Box II.

At this point, substituting Eqs. (6), (13), and (16) into Eq. (1), the micro-scale energy recasts as

$$\varepsilon_\varepsilon = \sum_{i=0}^{N-1} \frac{K_{E,i}}{2} \varepsilon^2 \left(\sqrt{T_i^2 + Q_i^2} - 2h \right)^2 \quad (17)$$

$$+ \frac{K_{B,i-1}}{2} \left\{ \frac{1}{\sqrt{T_i^2 + Q_i^2}} \left[T_i \cos \left(\frac{\delta_i}{2} \right) - Q_i \sin \left(\frac{\delta_i}{2} \right) \right] \right\}^2 \quad (18)$$

$$+ \frac{K_{T,i-1}}{2} \left\{ \frac{1}{\sqrt{T_i^2 + Q_i^2}} \left[T_i \cos \left(\frac{\delta_i}{2} \right) + Q_i \sin \left(\frac{\delta_i}{2} \right) \right] \right\}^2, \quad (19)$$

where, to avoid lengthy formulas, the quantities $T_i := R_i - \cos(\delta_i/2)$ and $Q_i := R_i \tan \Delta_i + 2h \cos(\delta_i/2)$ have been defined.

2.2. Micro–macro identification

We aim to formulate a one-dimensional continuum in the limit of vanishing ε . The continuum is then parameterized by the arclength $x \in [0, L]$ of the straight segment of length L connecting all points P_i , see the blue lines in Fig. 2. For the time being, owing to the rigorous asymptotic convergence results that we are going to prove in a forthcoming work, we assume the independent kinematic Lagrangian descriptors of the macro-model to be the functions

$$\chi : [0, L] \rightarrow \mathbb{E}^2, \quad \varphi : [0, L] \rightarrow \mathbb{R}. \quad (20)$$

The placement function χ places the 1D-continuum into \mathbb{E}^2 and is best suited to describe the points $p_i \in \mathbb{E}^2$ of the discrete system on a macro-level. To take into account also the effect of rotating S-shaped rigid bodies, the placement function is augmented by the *micro-rotation* function φ .¹ Recall that p_i and φ_i make up a minimal set of global generalized coordinates for the discrete system. We thus identify the discrete system with a one-dimensional continuum which can be classified as a micromorphic — Cosserat actually — continuum. It is also convenient to introduce the functions $\rho : [0, L] \rightarrow \mathbb{R}^+$ and $\vartheta : [0, L] \rightarrow \mathbb{R}$ in order to rewrite the tangent vector field χ' as

$$\chi'(x) = \rho(x) [\cos \vartheta(x) \mathbf{e}_x + \sin \vartheta(x) \mathbf{e}_y], \quad (21)$$

where prime denotes differentiation with respect to the reference arc length x . Thus, the quantity ρ corresponds to the norm of the tangent vector χ' . Such a quantity will be henceforth referred to as *stretch*. We explicitly remark that the current curve $\chi([0, L])$ can in general have a length $\int_0^L \rho \, dx$ different from L , as x is not an arc-length parametrization for χ but only for the reference placement $\chi_0(x) = x \mathbf{e}_x$. Fig. 3 elucidates graphically the kinematics of the continuum. Note that the choice of the maximal set of independent kinematic descriptors of the continuum will change several times throughout the paper. Table 1 reports the various maximal sets of independent kinematic descriptors adopted at continuum scale along the present paper ordered by adoption. Remark that, henceforth, when in the text we mention that the kinematics of the continuum is specified up to rigid translations, this is equivalent to say that $\chi(x_0)$ must be fixed for an arbitrary $x_0 \in [0, L]$ in order to completely specify the kinematics of the continuum. Note also that, in passing from the set n. 2 to the set n. 3 and from the set n. 3 to the set n. 4 in Table 1, a static condensation will be performed. The field r in Table 1 will be introduced later on in the paper.

For the Piola's micro–macro identification, we relate the discrete generalized coordinates p_i and φ_i of a single cell centered at node i with, respectively, the functions χ and φ evaluated at $x_i = i\varepsilon$,

¹ In the sequel, the field φ will be also called *attitude field* or *rotation angle field*

$$\begin{aligned} & \sin \alpha_{i-1}^T \\ &= \frac{\mathbf{d}_i^\perp \cdot (D_{i-1} - C_{i-1})}{\|D_{i-1} - C_{i-1}\|} \end{aligned} \quad (11)$$

$$= \frac{\varepsilon \left[-\cos\left(\frac{\delta_i}{2}\right) \mathbf{e}_{\vartheta_i+\Delta_i} + \sin\left(\frac{\delta_i}{2}\right) \mathbf{e}_{\vartheta_i+\Delta_i}^\perp \right] \cdot \left\{ \left[R_i - \cos\left(\frac{\delta_i}{2}\right) \right] \mathbf{e}_{\vartheta_i+\Delta_i} - \left[R_i \tan \Delta_i + 2h \cos\left(\frac{\delta_i}{2}\right) \right] \mathbf{e}_{\vartheta_i+\Delta_i}^\perp \right\}}{\|D_{i-1} - C_{i-1}\|} \quad (12)$$

$$= -\frac{\varepsilon}{\|D_{i-1} - C_{i-1}\|} \left\{ \cos\left(\frac{\delta_i}{2}\right) \left[R_i - \cos\left(\frac{\delta_i}{2}\right) \right] + \sin\left(\frac{\delta_i}{2}\right) \left[R_i \tan \Delta_i + 2h \cos\left(\frac{\delta_i}{2}\right) \right] \right\}, \quad (13)$$

Box I.

$$\begin{aligned} & \sin \alpha_{i-1}^B \\ &= -\frac{\mathbf{E}_i^\perp \cdot (D_{i-1} - C_{i-1})}{\|D_{i-1} - C_{i-1}\|} \end{aligned} \quad (14)$$

$$= \frac{-\varepsilon \left[-\cos\left(\frac{\delta_i}{2}\right) \mathbf{e}_{\vartheta_i+\Delta_i} - \sin\left(\frac{\delta_i}{2}\right) \mathbf{e}_{\vartheta_i+\Delta_i}^\perp \right] \cdot \left\{ \left[R_i - \cos\left(\frac{\delta_i}{2}\right) \right] \mathbf{e}_{\vartheta_i+\Delta_i} - \left[R_i \tan \Delta_i + 2h \cos\left(\frac{\delta_i}{2}\right) \right] \mathbf{e}_{\vartheta_i+\Delta_i}^\perp \right\}}{\|D_{i-1} - C_{i-1}\|} \quad (15)$$

$$= \frac{\varepsilon}{\|D_{i-1} - C_{i-1}\|} \left\{ \cos\left(\frac{\delta_i}{2}\right) \left[R_i - \cos\left(\frac{\delta_i}{2}\right) \right] - \sin\left(\frac{\delta_i}{2}\right) \left[R_i \tan \Delta_i + 2h \cos\left(\frac{\delta_i}{2}\right) \right] \right\}. \quad (16)$$

Box II.

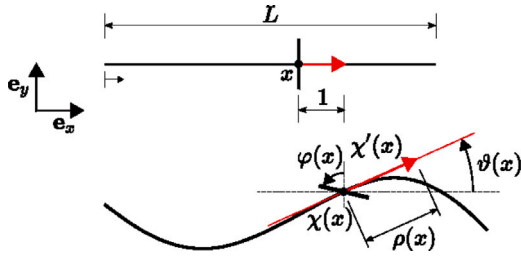


Fig. 3. Continuum model. Reference (top) and current (bottom) configurations along with the main kinematic quantities.

Table 1

Maximal sets of independent kinematic descriptors adopted at continuum scale along the present paper ordered by adoption.

	$\chi(\cdot)$	$\vartheta(\cdot)$	$\varphi(\cdot)$	$r(\cdot)$	$\Delta(\cdot)$	$\chi(\bar{x})$, with $\bar{x} \in [0, L]$ arbitrary
1.	X		X			X
2.			X	X	X	X
3.		X	X			X
4.			X			X

i.e. $\chi(x_i) = p_i$ and $\varphi(x_i) = \varphi_i$, with x_i the abscissa of node i along the middle line. For the asymptotic identification, we now need to expand the energy with respect to ε , so that we can re-write, up to higher order terms in ε , the deformation energy of each cell of the discrete system centered at node i as a function of the continuum generalized coordinates evaluated at x_i . Looking at Fig. 2, it is seen that the following relations hold true

$$\varphi_{i-1} = \Delta_i + \vartheta_i - \frac{\delta_i}{2}, \quad \varphi_i = \Delta_i + \vartheta_i + \frac{\delta_i}{2}, \quad (22)$$

which imply the following expressions for the quantities Δ_i and δ_i

$$\Delta_i = \frac{\varphi_{i-1} - \vartheta_i}{2} + \frac{\varphi_i - \vartheta_i}{2}, \quad \delta_i = (\varphi_i - \vartheta_i) - (\varphi_{i-1} - \vartheta_i). \quad (23)$$

We now expand in Taylor series centered in x_i the fields φ and χ uniquely specifying the kinematics of the continuum

$$\varphi_{i+1} - \varphi_i = \varepsilon \varphi'(x_i) + o(\varepsilon), \quad p_i - p_{i-1} = \varepsilon \chi'(x_i) + o(\varepsilon). \quad (24)$$

Plugging the above expansion in Eq. (23), we get the following ε -approximations for the quantities Δ_i and δ_i

$$\Delta_i = [\varphi(x_i) - \vartheta(x_i)] + o(\varepsilon^0), \quad \delta_i = \varepsilon \varphi'(x_i) + o(\varepsilon). \quad (25)$$

At this point, we can easily see that the formula (21) is nothing but the continualization of the expression

$$p_i - p_{i-1} = \|p_i - p_{i-1}\| [\cos \vartheta_i(x) \mathbf{e}_x + \sin \vartheta_i(x) \mathbf{e}_y]. \quad (26)$$

Indeed, dividing (26) by ε , plugging (24) in (26) considering $\vartheta_i = \vartheta(x_i)$, and letting $\varepsilon \rightarrow 0$, we get (21), where $\rho(x_i) = \lim_{\varepsilon \rightarrow 0} \|p_i - p_{i-1}\|/\varepsilon$. In particular, note that we have $\rho_i = \rho(x_i) + o(\varepsilon)$. Thus, plugging the expressions in Eq. (25) into the deformation energy (19) of the discrete model, we get

$$\mathcal{E}_\varepsilon = \sum_{i=0}^{N-1} \frac{K_{E,i}}{2} \varepsilon^2 \left(\sqrt{\tilde{T}_i^2 + \tilde{Q}_i^2} - 2h + o(\varepsilon) \right)^2 \quad (27)$$

$$+ \frac{K_{B,i-1}}{2} \left\{ \frac{1}{\sqrt{\tilde{T}_i^2 + \tilde{Q}_i^2 + o(\varepsilon)}} \left\{ [1 + o(\varepsilon)] (\tilde{T}_i + o(\varepsilon)) - \left[\frac{\varphi'(x_i)}{2} + o(\varepsilon^2) \right] (\tilde{Q}_i + o(\varepsilon)) \right\} \right\}^2 \quad (28)$$

$$+ \frac{K_{T,i-1}}{2} \left\{ \frac{1}{\sqrt{\tilde{T}_i^2 + \tilde{Q}_i^2 + o(\varepsilon)}} \left\{ [1 + o(\varepsilon)] (\tilde{T}_i + o(\varepsilon)) + \left[\frac{\varphi'(x_i)}{2} + o(\varepsilon^2) \right] (\tilde{Q}_i + o(\varepsilon)) \right\} \right\}^2, \quad (29)$$

where, to avoid lengthy formulas, the quantities $\tilde{T}_i := R_i - 1$ and $\tilde{Q}_i := R_i \tan \Delta_i + 2h$ have been defined.

At this point, it is necessary to specify a scaling law for the stiffnesses. The stiffness scaling laws, which determine how micro-scale stiffnesses depend upon the number of cells, are specified by means of power laws as

$$K_{E,i} = \tilde{K}_{E,i} \varepsilon^{-1}, \quad K_{T(B),i} = \tilde{K}_{T(B),i} \varepsilon^{-1}, \quad (30)$$

where $\tilde{K}_{E,i}$ and $\tilde{K}_{T(B),i}$ do not depend on ε . Note that, according to the scaling (30), we have $K_{B(T),i}/K_{E,i} = O(\varepsilon^0)$, which means that neither rotational springs (both of them, top and bottom) nor extensional springs have negligible stiffnesses asymptotically for ε tending to zero. Once plugged in Eq. (29), the scaling laws above give

$$\mathcal{E}_\varepsilon = \sum_{i=0}^{N-1} \frac{\varepsilon \tilde{K}_{E,i}}{2} \left[\sqrt{(R_i - 1)^2 + (R_i \tan \Delta_i + 2h)^2} - 2h + o(\varepsilon) \right]^2 \quad (31)$$

$$+ \frac{\varepsilon \tilde{K}_{B,i-1}}{2} \left\{ \frac{\varepsilon^{-1} (R_i - 1) - \varphi'(x_i) \left(\frac{R_i \tan \Delta_i + 2h}{2} \right)}{\sqrt{(R_i - 1)^2 + (R_i \tan \Delta_i + 2h)^2}} + o(\varepsilon^0) \right\}^2 \quad (32)$$

$$+ \frac{\varepsilon \tilde{K}_{T,i-1}}{2} \left\{ \frac{\varepsilon^{-1} (R_i - 1) + \varphi'(x_i) \left(\frac{R_i \tan \Delta_i + 2h}{2} \right)}{\sqrt{(R_i - 1)^2 + (R_i \tan \Delta_i + 2h)^2}} + o(\varepsilon^0) \right\}^2. \quad (33)$$

Let us define the variable $r_i = \varepsilon^{-1} (R_i - 1)$, which allows us to rewrite the previous expression as

$$\mathcal{E}_\varepsilon = \sum_i \frac{\varepsilon \tilde{K}_{E,i}}{2} \left[\sqrt{\varepsilon^2 r_i^2 + [(1 + \varepsilon r_i) \tan \Delta_i + 2h]^2} - 2h + o(\varepsilon) \right]^2 \quad (34)$$

$$+ \frac{\varepsilon \tilde{K}_{B,i-1}}{2} \left\{ \frac{r_i - \varphi'(x_i) \frac{(1 + \varepsilon r_i) \tan \Delta_i + 2h}{2}}{\sqrt{\varepsilon^2 r_i^2 + [(1 + \varepsilon r_i) \tan \Delta_i + 2h]^2}} + o(\varepsilon^0) \right\}^2 \quad (35)$$

$$+ \frac{\varepsilon \tilde{K}_{T,i-1}}{2} \left\{ \frac{r_i + \varphi'(x_i) \frac{(1 + \varepsilon r_i) \tan \Delta_i + 2h}{2}}{\sqrt{\varepsilon^2 r_i^2 + [(1 + \varepsilon r_i) \tan \Delta_i + 2h]^2}} + o(\varepsilon^0) \right\}^2. \quad (36)$$

Note that, for each cell centered at node i , the variable r_i is a kinematic descriptor independent of the variables Δ_i and δ_i , which are also independent. Thus, the kinematics of the system is completely described, as an instance, by the triple of independent kinematic descriptors r_i , Δ_i , and φ_i , complemented by the placement of one node along the middle line. Let us adopt this kinematics for the discrete system and, accordingly, also for the sought continuum limit. At the continuum level, the quantities r_i and Δ_i become the functions $r : [0, L] \rightarrow \mathbb{R}$ and $\Delta : [0, L] \rightarrow \mathbb{R}$, respectively.

2.3. Macro-model

The continuum limit is now obtained by letting $\varepsilon \rightarrow 0$ and reminding that the summation in Eq. (36) turns into an integral according to $\sum_i f(x_i) \varepsilon \xrightarrow{\varepsilon \rightarrow 0} \int_0^L f \, dx$, where f is a real valued function defined on $[0, L]$. Limiting ourselves to study only cases in which the energy of the continuous limit is finite, it is obtained that $r_i = o(\varepsilon^0)$, namely $\rho_i \cos \Delta_i - 1 = o(\varepsilon)$. In conclusion, the deformation energy of the limit continuum reads as

$$\mathcal{E} = \int_0^L \left\{ \frac{\tilde{K}_E}{2} \left[\sqrt{(\tan \Delta + 2h)^2} - 2h \right]^2 + \frac{\tilde{K}_B}{2} \left[\frac{r - \varphi' \frac{\tan \Delta + 2h}{2}}{\sqrt{(\tan \Delta + 2h)^2}} \right]^2 + \frac{\tilde{K}_T}{2} \left[\frac{r + \varphi' \frac{\tan \Delta + 2h}{2}}{\sqrt{(\tan \Delta + 2h)^2}} \right]^2 \right\} dx, \quad (37)$$

while the condition $r_i = o(\varepsilon^0)$ reads at the continuum level as $\rho \cos \Delta = 1$ almost everywhere in $[0, L]$.

The stiffnesses \tilde{K}_E , \tilde{K}_B , and \tilde{K}_T in Eq. (37) are non-negatively valued functions of the abscissa $x \in [0, L]$ such that $\tilde{K}_E(x_i) = \tilde{K}_{E,i}$, $\tilde{K}_B(x_i) = \tilde{K}_{B,i}$, and $\tilde{K}_T(x_i) = \tilde{K}_{T,i}$, respectively.

Remark that the continuum field variable Δ can be expressed in terms of the quantities ϑ and φ as $\Delta = \varphi - \vartheta$ according to the continualization of Eq. (25). In the language of continuum mechanics, the quantity Δ thus represents the so-called *shear deformation* of the 1D continuum. It is worth to note also that the quantities Δ and φ are sufficient to retrieve the current deformed curve of the continuum once the placement of a point of the continuum is known. Indeed, the quantity ϑ is obtained as $\vartheta = \varphi - \Delta$. The quantity ρ is instead obtained by the constraint (38) as

$$\rho = 1 / \cos \Delta \quad (39)$$

and, finally, the placement function is retrieved by integrating Eq. (21). The above expression (39) for the quantity ρ suggests that $\rho \geq 1$ for $\varphi - \vartheta \in [-\pi/2, \pi/2]$, which means that the duoskelion beam, because of the scaling laws, is incompressible. This kind of behavior goes under the name of *mechanical diode*.

By plugging the condition $r_i = o(\varepsilon^0)$ and the asymptotic expansion $\delta_i = \varepsilon \varphi'(x_i) + o(\varepsilon)$ obtained in Eq. (25) into $\|D_{i-1} - C_{i-1}\|$ in Eq. (6), we get Eqs. (40)–(42) given in Box III, which suggests that, at the continuum level, the quantity $\tan \Delta(x_i) + 2h$ stands for the current signed length of the extensional spring on the left of node i , normalized with respect to the cell length ε . Since in the reference configuration the equality $\Delta = 0$ holds true, the quantity $\tan \Delta + 2h$ is greater than zero in such a configuration. To pass from a positive value of such a signed length to a negative one, one must hence pass through a completely compressed configuration where $\tan \Delta + 2h = 0$. Such a configuration is pathological, because the two last addends of the continuum energy density in (37) blow up to infinity when $\tan \Delta + 2h \rightarrow 0$. It is thus reasonable limiting ourselves to study only cases where $\tan \Delta + 2h \geq 0$. In such a case, the energy (37) reads as

$$\mathcal{E} = \int_0^L \left[\frac{\tilde{K}_E}{2} \tan^2 \Delta + \frac{\tilde{K}_B}{2} \left(\frac{r - \varphi' \frac{\tan \Delta + 2h}{2}}{\tan \Delta + 2h} \right)^2 + \frac{\tilde{K}_T}{2} \left(\frac{r + \varphi' \frac{\tan \Delta + 2h}{2}}{\tan \Delta + 2h} \right)^2 \right] dx, \quad (43)$$

which, defining a new internal variable $\tilde{r} = \frac{r}{\tan \Delta + 2h}$ substituting r in the set of independent kinematic descriptors, can be further recast as

$$\mathcal{E} = \int_0^L \left[\frac{\tilde{K}_E}{2} \tan^2 \Delta + \frac{\tilde{K}_B}{2} \left(\tilde{r} - \frac{\varphi'}{2} \right)^2 + \frac{\tilde{K}_T}{2} \left(\tilde{r} + \frac{\varphi'}{2} \right)^2 \right] dx. \quad (44)$$

It is worth to be remarked that the aspect ratio of the unit cell h does no more appear in the deformation energy (44) after the hypothesis $\tan \Delta + 2h \geq 0$.

We now address the static condensation of the variable \tilde{r} . At first, we note that the dependence of the deformation energy density \mathcal{E} in Eq. (44) upon the newly introduced variable \tilde{r} is only algebraic. Additionally, the variable \tilde{r} does not appear in the constraint (38). Therefore, conditions for the stationarity of the energy functional \mathcal{E} with respect to \tilde{r} are simply obtained as

$$0 = \frac{\partial \mathcal{E}}{\partial \tilde{r}} = \tilde{K}_B \left(\tilde{r} - \frac{\varphi'}{2} \right) + \tilde{K}_T \left(\tilde{r} + \frac{\varphi'}{2} \right), \quad (45)$$

which can be easily solved, giving the following expression for the variable \tilde{r}

$$\tilde{r} = \frac{\tilde{K}_B - \tilde{K}_T}{2(\tilde{K}_B + \tilde{K}_T)} \varphi'. \quad (46)$$

Note that the energy functional (44) is convex with respect to \tilde{r} . Therefore, the expression for \tilde{r} in the equation above actually gives not just a stationary point, but a minimum one. Note also that, when $\tilde{K}_B(x) = \tilde{K}_T(x)$, i.e. the duoskelion is *balanced* at x , the variable \tilde{r} is null

$$\|D_{i-1} - C_{i-1}\| = \varepsilon \sqrt{\left\{ \left[R_i - \cos\left(\frac{\delta_i}{2}\right) \right]^2 + \left[R_i \tan \Delta_i + 2h \cos\left(\frac{\delta_i}{2}\right) \right]^2 \right\}} \quad (40)$$

$$\stackrel{r_i = o(\varepsilon^0)}{=} \varepsilon \sqrt{\left\{ \left[1 + o(\varepsilon) - \cos\left(\frac{\delta_i}{2}\right) \right]^2 + \left[(1 + o(\varepsilon)) \tan \Delta_i + 2h \cos\left(\frac{\delta_i}{2}\right) \right]^2 \right\}} \quad (41)$$

$$\stackrel{\text{Eq. (25)}}{=} \varepsilon |\tan \Delta_i + 2h| + o(\varepsilon), \quad (42)$$

Box III.

at x . Back-substituting Eq. (46) into the continuum deformation energy in Eq. (44), we get the following expression for the deformation energy of the continuum limit

$$\mathcal{E} = \int_0^L \frac{\tilde{K}_E}{2} \tan^2 \Delta + \frac{\tilde{K}_R}{2} \varphi'^2 dx, \quad (47)$$

with

$$\tilde{K}_R = \tilde{K}_B \left(\frac{\tilde{K}_T}{\tilde{K}_B + \tilde{K}_T} \right)^2 + \tilde{K}_T \left(\frac{\tilde{K}_B}{\tilde{K}_B + \tilde{K}_T} \right)^2 = \frac{\tilde{K}_B \tilde{K}_T}{\tilde{K}_B + \tilde{K}_T}. \quad (48)$$

Note that, when $\tilde{K}_R \rightarrow 0$, the energy turns into that of a *cable* where no energy is accumulated in bending. In conclusion, we have got at continuum level a one-dimensional Cosserat continuum (Eremeyev and Pietraszkiewicz, 2012; Altenbach and Eremeyev, 2009; Altenbach et al., 2013)—a non-linear generalization of the Timoshenko–Ehrenfest beam model (Elishakoff, 2020; Battista et al., 2018; Della Corte et al., 2019; Harsch and Eugster, 2020) actually, see (47)—internally constrained by Eq. (38). Looking at the energy (47), the essential boundary data that we may want to assign — not necessarily all of them — are $\chi(0) = \chi_0$ (or its projection onto a direction), $\chi(L) = \chi_L$ (or its projection onto a direction), $\varphi(0) = \varphi_0$, and $\varphi(L) = \varphi_L$.

3. Equilibrium equations for duoskelion beams subjected to axial loads

In this Section, we begin the study of equilibrium configurations of duoskelion beams subjected to axial loads. After having introduced an Extended Lagrangian formulation, we write the equilibrium equations and, subsequently, we perform a kinematic reduction. Such a kinematic reduction allows to characterize equilibria only in terms of the attitude field φ . Additionally, the reduction to an optimization problem involving a single field permits the application of the so-called Weierstrass' qualitative study of solutions.

We now choose as new set of independent kinematic descriptors of the system the fields ϑ and φ , once rigid translations of the continuum are blocked. The static problem that we want to study considers for the placement function hinge conditions $\chi(0) = \mathbf{0}$ at the left end of the beam, prescribed axial placement $\chi(L) \cdot \mathbf{e}_x = L + u_L$ at the right end — the transverse right end displacement is left free — and, possibly, clamping conditions $\varphi(0) = \varphi_0$ and/or $\varphi(L) = \varphi_L$ at beam's ends on the attitude field.² The problem that shall be studied can be thus summarized as follows

Find the stationary configurations $(\vartheta^*(\cdot), \varphi^*(\cdot))$ of \mathcal{E} such that $[\chi(L) - \chi(0)] \cdot \mathbf{e}_x = L + u_L$, with $u_L \in \mathbb{R}$, and fulfilling B.C.'s on φ . (49)

We note that it is possible to write the constraint $[\chi(L) - \chi(0)] \cdot \mathbf{e}_x = L + u_L$ in terms of the quantities ϑ and φ . Indeed, the equality chain

$$[\chi(L) - \chi(0)] \cdot \mathbf{e}_x = \int_0^L (\chi' \cdot \mathbf{e}_x) dx \stackrel{\text{Eq. (21)}}{=} \int_0^L \rho \cos \vartheta dx$$

² These conditions shall be referred to in the sequel as *B.C.'s on φ* .

$$\stackrel{\text{Eq. (38)}}{=} \int_0^L \frac{\cos \vartheta}{\cos(\varphi - \vartheta)} dx \quad (50)$$

leads to the following expression of the constraint

$$\int_0^L \frac{\cos \vartheta}{\cos(\varphi - \vartheta)} dx = L + u_L. \quad (51)$$

In conclusion, the problem that shall be studied can be summarized as follows

Find the stationary configurations $(\vartheta^*(\cdot), \varphi^*(\cdot))$ of \mathcal{E}

such that $\int_0^L \frac{\cos \vartheta}{\cos(\varphi - \vartheta)} dx = L + u_L$, with $u_L \in \mathbb{R}$,

and fulfilling B.C.'s on φ . (52)

3.1. Augmented Lagrangian formulation

To enforce the constraint $\int_0^L \frac{\cos \vartheta}{\cos(\varphi - \vartheta)} dx = L + u_L$ in the problem (52), we define the augmented energy functional \mathcal{E}^A

$$\mathcal{E}^A = \int_0^L \frac{\tilde{K}_E}{2} \tan^2(\varphi - \vartheta) + \frac{\tilde{K}_R}{2} \varphi'^2 dx - \lambda \left[\int_0^L \frac{\cos \vartheta}{\cos(\varphi - \vartheta)} dx - (L + u_L) \right], \quad (53)$$

so that the problem (52) recasts as

Find the stationary triples $(\vartheta^*(\cdot), \varphi^*(\cdot), \lambda^*)$ of \mathcal{E}^A fulfilling B.C.'s on φ . (54)

Note that the real quantity λ is not a field.

3.2. Reduced Euler–Lagrange equations

Let us now assume λ to be fixed. Therefore, a family of tuples $(\vartheta^*(\cdot), \varphi^*(\cdot))$ is sought for a given λ , such that the triples $(\vartheta^*(\cdot), \varphi^*(\cdot), \lambda)$ are solutions of problem (54). Note that the quantity λ is nothing but the external force applied on the right boundary of the continuum. Indeed, up to the constant quantity λu_L , the quantity that has been subtracted from \mathcal{E} in (47) to get \mathcal{E}^A in (53) is nothing but the external work done by the external force λ on the right end displacement. A positive λ stands for a traction force, while a negative λ stands for a compression force.

Recall that any constant, i.e. known, real quantity can be added to a function without changing its stationary points and their nature. Recall also that multiplying a function by a positive constant does not change its stationary points and their nature. Therefore, for the sake of simplicity, we define a new augmented energy functional \mathcal{E}_A according to the following expression

$$\mathcal{E}_A := \int_0^L \frac{1}{2} \tan^2(\varphi - \vartheta) + \frac{K}{2} \varphi'^2 dx - \Lambda \left[\int_0^L \frac{\cos \vartheta}{\cos(\varphi - \vartheta)} dx \right] \quad (55)$$

$$= \int_0^L \left[\frac{1}{2} \tan^2(\varphi - \vartheta) + \frac{K}{2} \varphi'^2 - \frac{\Lambda \cos \vartheta}{\cos(\varphi - \vartheta)} \right] dx, \quad (56)$$

obtained by subtracting the known real quantity $\lambda(u_L - L)$ from the energy functional (53) and then dividing it by \tilde{K}_E . Remark that the quantity \tilde{K}_E is always greater than zero. The quantities K and Λ in (56) have been defined as $K = \tilde{K}_R/\tilde{K}_E$ and $\Lambda = \lambda/\tilde{K}_E$, respectively. At this point, the problem that we seek to solve reads as

Find, for a given Λ , the stationary configurations $(\vartheta^*(\cdot), \varphi^*(\cdot))$ of \mathcal{E}_Λ fulfilling B.C.'s on φ . (57)

We now address the static condensation of the variable ϑ . Note that the dependence of the deformation energy density $\tilde{\mathcal{E}}_\Lambda$ in Eq. (56) upon the variable ϑ is only algebraic. Enforcing the stationarity of the energy \mathcal{E}_Λ with respect to the quantity ϑ , we obtain

$$0 = \frac{\partial \tilde{\mathcal{E}}_\Lambda}{\partial \vartheta} = \Lambda \frac{\sin \varphi}{\cos^2(\varphi - \vartheta)} - \frac{\tan(\varphi - \vartheta)}{\cos^2(\varphi - \vartheta)}. \quad (58)$$

Assuming that $\cos(\varphi - \vartheta) \neq 0$, from Eq. (58) we get the following relationship

$$\tan(\varphi - \vartheta) = \Lambda \sin \varphi, \quad (59)$$

which gives a closed form expression for $\tan(\varphi - \vartheta)$ in terms of the field φ . Recalling that by elementary trigonometric relationships the following equality holds

$$\cos(\vartheta) = \cos(\varphi - \vartheta) \cos(\varphi) + \sin(\varphi - \vartheta) \sin(\varphi) \quad (60)$$

and using (59), it is easily seen that

$$\frac{\cos \vartheta}{\cos(\varphi - \vartheta)} = \cos \varphi + \Lambda \sin^2 \varphi. \quad (61)$$

Plugging the expressions (59) and (61) into the energy \mathcal{E}_Λ in (56), we get the following expression for \mathcal{E}_Λ

$$\mathcal{E}_\Lambda = \int_0^L \left[\frac{K}{2} \varphi'^2 + V(\varphi) \right] dx, \quad (62)$$

where the function V has been defined as

$$V = -\Lambda \left(\cos \varphi + \frac{\Lambda}{2} \sin^2 \varphi \right). \quad (63)$$

In conclusion, we have expressed the energy functional \mathcal{E}_Λ as a function of the field φ only. Defining a new non-dimensional space variable $\xi = x/L_0 \in [0, L/L_0]$ and the coefficient $\tilde{K} = K/L_0^2$, the augmented energy functional \mathcal{E}_Λ reads as

$$\mathcal{E}_\Lambda = \int_0^{L/L_0} \left[\frac{\tilde{K}}{2} \varphi'^2 + V(\varphi) \right] d\xi, \quad (64)$$

where prime denotes differentiation with respect to the non-dimensional abscissa ξ . Henceforth, the prime symbol will denote differentiation with respect to the non-dimensional abscissa ξ . At this point, problem (57) recasts as

Find the fields $\varphi^*(\cdot)$ fulfilling B.C.'s on φ

that, for a given Λ , make stationary \mathcal{E}_Λ . (65)

Henceforth, the stiffnesses \tilde{K} will be assumed to be independent of the abscissa ξ . Equating to zero the first variation of the functional \mathcal{E}_Λ with respect to the variable φ , by straightforward computations which include an integration by parts, we get the following differential equation for the unknown field φ in the bulk of the beam

$$-\tilde{K} \varphi'' + \frac{\partial V}{\partial \varphi} = 0 \quad (66)$$

while, at the boundaries, i.e. $\xi \in \{0, L/L_0\}$, we get the condition $\varphi' \delta \varphi = 0$. Defining $\tilde{V} = V/\tilde{K}$, we obtain from Eq. (66) the following differential equation for the attitude field

$$\varphi'' - \frac{\partial \tilde{V}}{\partial \varphi} = 0. \quad (67)$$

3.3. Uniform equilibrium solutions

Let us look for solutions of problem (65) consisting into uniform deformations. To this end, let us fix $\varphi' = 0$ and assume that no boundary conditions are given on the angle φ . Then, the dependence of the deformation energy density $\tilde{\mathcal{E}}_\Lambda$ in Eq. (62) upon the variable φ is only algebraic and the Euler–Lagrange equation for φ associated to the energy (62) reads as

$$0 = \frac{\partial \tilde{\mathcal{E}}_\Lambda}{\partial \varphi} = -\Lambda \sin \varphi (\Lambda \cos \varphi - 1), \quad (68)$$

which admits as solution either $\varphi = 0$ or $\cos \varphi = 1/\Lambda$, this last being equivalent to $\varphi = \pm \arccos(1/\Lambda)$.

Note that $\varphi = \pm \arccos(1/\Lambda)$ is indeed a solution of Eq. (68) only if $|\Lambda| > 1$. Therefore, we are led to the following result. When $|\Lambda| < 1$, the only uniform deformation solving problem (65) is such that $\varphi = 0$, it is namely the undeformed configuration — note that $\vartheta = 0$ from Eq. (59) and that $\rho = 1$ from Eq. (39). When $|\Lambda| > 1$, there exist two non-trivial solutions of problem (65) consisting of uniform deformations different from the undeformed configuration, namely $\varphi = \pm \arccos(1/\Lambda)$.

In the non-trivial case $\varphi = \pm \arccos(1/\Lambda)$, the quantity ϑ can be computed from Eq. (59) as

$$\tan \left[\pm \arccos \left(\frac{1}{\Lambda} \right) - \vartheta \right] = \Lambda \sin \left[\pm \arccos \left(\frac{1}{\Lambda} \right) \right]. \quad (69)$$

We note that, when $\vartheta = 0$, the previous equation can be rewritten as

$$\pm \tan \left[\arccos \left(\frac{1}{\Lambda} \right) \right] = \pm \Lambda \sin \left[\arccos \left(\frac{1}{\Lambda} \right) \right], \quad (70)$$

which is always satisfied for $|\Lambda| > 1$. Indeed

$$\tan \left[\arccos \left(\frac{1}{\Lambda} \right) \right] = \frac{\sin \left[\arccos \left(\frac{1}{\Lambda} \right) \right]}{\cos \left[\arccos \left(\frac{1}{\Lambda} \right) \right]} = \Lambda \sin \left[\arccos \left(\frac{1}{\Lambda} \right) \right]. \quad (71)$$

Therefore, all the solutions of problem (65) being uniform deformations exhibit a rectilinear current shape. Regarding the elongation ρ , in the cases $\varphi = \pm \arccos(1/\Lambda) \in [-\pi/2 + 2k\pi, \pi/2 + 2k\pi]$, $k \in \mathbb{Z}$ —which require $\Lambda \geq 1$ — it is uniform along the domain and its value is

$$\rho = \frac{1}{\cos \varphi} = \Lambda \geq 1 \quad (72)$$

while, in the cases $\varphi = \pm \arccos(1/\Lambda) \in [\pi/2 + 2k\pi, 3/2\pi + 2k\pi]$, $k \in \mathbb{Z}$ —which require $\Lambda \leq -1$ — it is uniform along the domain and its value is

$$\rho = \frac{1}{\cos \varphi} = \Lambda \leq -1. \quad (73)$$

However, this last equality cannot be fulfilled as, by definition, we have $\rho \geq 0$. In conclusion, for $\Lambda \leq 1$, no deformation is observed, i.e. only the zero solution $\varphi = 0$ exists — which implies $\rho = 1$ — while for $\Lambda > 1$ we have also the solution $\varphi = \pm \arccos(1/\Lambda) \in [-\pi/2 + 2k\pi, \pi/2 + 2k\pi]$, $k \in \mathbb{Z}$, which implies $\rho = \Lambda$. This kind of behavior can be categorized not only under the name of *mechanical diode*, which is due to the fact that, as mentioned earlier, the beam can only be elongated and not shortened. Actually, the fact that there exists a threshold for Λ below which the axial force has no effect on the deformation of the beam can also be regarded as duoskelion beams behaving like mechanical switches. It is worth noting that the results of this section are in perfect agreement with those presented in a previous article introducing duoskelion structures (Barchiesi et al., 2021a) (see Fig. 6, p. 4 of the cited reference), where numerical computations were performed using the same discrete model utilized in Section 6.

Recall that, in the foregoing, the assumption $\tan \Delta + 2h \geq 0$ was made. Taking into account the fact that $\vartheta = 0$, such an inequality recasts as $\tan \varphi + 2h \geq 0$ or, equivalently, as

$$-\frac{\pi}{2} < -\arctan(2h) \leq \varphi. \quad (74)$$

The inequality above is trivially verified for $\varphi = 0$, while the range of h for such an inequality to hold in the non-trivial cases $\varphi = \pm \arccos(1/\Lambda)$

should be analyzed. At first, note that $-\arctan(2h) < 0$. By means of elementary trigonometric relationships, the inequality

$$-\arctan(2h) \leq \pm \arccos(1/\Lambda) \quad (75)$$

recasts as

$$\Lambda^2 - 1 \leq 4h^2. \quad (76)$$

All previous discussions will be re-interpreted in the light of the Weierstrass' qualitative study presented in the next section. While in studying uniform solutions we have not given essential boundary conditions on φ , in the next subsection we are going to prescribe the essential boundary condition $\varphi = 0$ at the left and right ends of the beam. In such a case, the only uniform equilibrium solution is the null one, of which we study the stability.

3.4. Linear stability analysis

We know that, for all Λ 's, the function $\varphi(\xi)$, such that $\varphi(\xi) = 0$ for all $\xi \in [0, 1]$, is a solution to the following problem

Find the fields $\varphi^*(\cdot)$ that, for a given Λ , make stationary

$$\int_0^{L/L_0} \left[\frac{1}{2} \varphi'^2 + \tilde{V} \right] d\xi$$

such that $\varphi(\xi = 0) = \varphi(\xi = 1) = 0$ (77)

to which we have reduced our initial problem (cfr. (65), we are here considering a notable set of boundary conditions on φ), exploiting the Euler–Lagrange equation for the field $\vartheta(\xi)$ and the internal constraint $\rho(\xi) \cos \Delta(\xi) = 1$. Remark that the functional appearing in the problem above vanishes for $\varphi(\xi) = 0$. Therefore, if it is positive — for a given Λ — for all the sufficiently regular and small fields $\varphi(\xi)$ different from zero fulfilling the boundary conditions $\varphi(\xi = 0) = \varphi(\xi = 1) = 0$, i.e. kinematically admissible, it means that the zero solution does not only make stationary the energy, but it is also a local minimum among the kinematically admissible fields. The solution $\varphi(\xi) = 0$ is in that case a locally stable solution of the problem (77).

In this subsection we shall study the linear stability (a special case of local stability) of the zero solution to problem (77). To check whether, for a given Λ , the condition above is fulfilled, we approximate the function $\tilde{V}(\varphi)$ — appearing in the density of the augmented energy functional — in the neighborhood of $\varphi = 0$ by means of a Taylor expansion truncated at the second order in φ . This leads to the approximation of the density of the augmented energy functional through a quadratic function — specifically, without mixed and linear terms — of φ' and φ . For the sake of simplicity, we shall henceforth consider a particular ratio L/L_0 , i.e. $L/L_0 = 1$.

We are considering small perturbations of the uniform solution $\varphi = 0$, such that the following Taylor approximation of \tilde{V} , truncated at second order, can be utilized

$$\tilde{V} \approx \tilde{V} \Big|_{\varphi=0} + \frac{\partial \tilde{V}}{\partial \varphi} \Big|_{\varphi=0} \varphi + \frac{1}{2} \frac{\partial^2 \tilde{V}}{\partial \varphi^2} \Big|_{\varphi=0} \varphi^2. \quad (78)$$

Since

$$\frac{\partial \tilde{V}}{\partial \varphi} \Big|_{\varphi=0} = 0, \quad (79)$$

when only solutions to problem (77) being small perturbations of the uniform solution $\varphi = 0$ are sought, problem (77) can be replaced by the following one

Find the fields $\varphi^*(\cdot)$ that, for a given Λ , make stationary

$$\int_0^1 \left(\frac{1}{2} \varphi'^2 + \frac{1}{2} \frac{\partial^2 \tilde{V}}{\partial \varphi^2} \Big|_{\varphi=0} \varphi^2 \right) d\xi$$

such that $\varphi(0) = \varphi(1) = 0$. (80)

As mentioned above, since the augmented energy functional in (80) is equal to zero for the solution $\varphi = 0$, we want to prove, for a given Λ , that the augmented energy functional in (80) is positive for all the sufficiently regular and small fields φ 's different from zero fulfilling the boundary conditions $\varphi(0) = \varphi(1)$. This is a sufficient condition to prove the linear stability of the zero solution. Without loss of generality, we can assume that the integral between of the quantity φ^2 is equal to one. Therefore, we seek to prove that

$$C_P^2 := \inf_{\varphi \in W_0^{1,2}([0,1]) \text{ s.t. } \int_0^1 \varphi^2 d\xi = 1} \int_0^1 \varphi'^2 d\xi > - \frac{\partial^2 \tilde{V}}{\partial \varphi^2} \Big|_{\varphi=0}. \quad (81)$$

The quantity C_P^2 in (81) is the inverse of the optimal — i.e. sharpest — value of the constant C in the Poincaré inequality $\|\varphi\|_{L^p(\Omega)} \leq C \|\nabla \varphi\|_{L^p(\Omega)} \forall \varphi \in W_0^{1,p}(\Omega)$ for the 1D domain $\Omega = [0, 1]$ and the norm L^2 , i.e. $p = 2$.³ In our case, the inverse of the optimal constant is equal to π^2 . We can thus conclude that $0 < \Lambda < 1$ is a sufficient condition for $\varphi = 0$ to be a linearly stable solution. More generally, the condition $-\Lambda(\Lambda - 1)/\tilde{K} + \pi^2 > 0$, is a sufficient condition for $\varphi = 0$ to be a linearly stable equilibrium solution. Therefore, when this condition is fulfilled, for the considered boundary conditions, only non-uniform equilibrium solutions, that we address in the next section, can be linearly unstable.

In Appendix A, we have included an alternative proof of these conclusions, which makes use of the direct methods of the calculus of variations.

4. Non-uniform equilibrium solutions: problem statement

Henceforth, given the ordinary differential Eq. (67) governing the field $\varphi(\xi)$ in the bulk of the continuum and the boundary condition $\varphi' \delta \varphi = 0$, we shall be looking for solutions of the boundary value problem

$$\varphi'' - \frac{\partial \tilde{V}}{\partial \varphi} = 0 \text{ on } [0, L/L_0] \quad \varphi(0) = 0, \varphi(L/L_0) = 0 \quad (82)$$

and of the mixed problem

$$\varphi'' - \frac{\partial \tilde{V}}{\partial \varphi} = 0 \text{ on } [0, L/L_0] \quad \varphi(0) = 0, \varphi'(L/L_0) = 0 \quad (83)$$

which correspond to a beam clamped on both sides and a beam clamped only on the left end side and free on the other, respectively.

4.1. Equivalent dynamical system

Eq. (67) can be equivalently recast in the form of a first-order dynamical system

$$\begin{cases} \frac{\partial \varphi}{\partial \xi} = y \\ \frac{\partial y}{\partial \xi} = \frac{\partial \tilde{V}}{\partial \varphi}, \end{cases} \quad (84)$$

³ The inverse of the optimal constant in the Poincaré inequality is found as Heimonen et al. (2001)

$$\inf_{W_0^{1,p}(\Omega)} \{ \|\nabla \varphi\|_{L^p(\Omega)} : \|\varphi\|_{L^p(\Omega)} = 1 \},$$

which is, clearly, strictly positive. It can be proven that, for $p = 2$, the infimum takes the value λ_1^{-1} , with $-\lambda_1$ being the first eigenvalue of the Laplacian operator with homogeneous Dirichlet conditions, namely the smallest real number such that the following Dirichlet problem admits non-vanishing solutions in $W_0^{1,2}(\Omega)$

$$-\Delta \varphi = \lambda \varphi \quad \text{in } \Omega \\ \varphi = 0 \quad \text{on } \partial \Omega.$$

Note that, in our case, the inverse of the optimal constant can be found as

$$\inf_{W_0^{1,2}([0,1])} \left\{ \int_0^1 \varphi'^2 dx : \int_0^1 \varphi^2 dx = 1 \right\}.$$

which means that a solution $\varphi(\xi)$ of Eq. (67) is a trajectory of the Lipschitz-continuous dynamical system (84). It is worth remarking that if, instead of regarding ξ as a space variable, we consider it to be a time variable, we can interpret (84) as the well-known Hamiltonian dynamical system describing the motion of a particle submitted to the potential $-\tilde{V}$, whose prime integral, i.e. the quantity which is conserved over trajectories, is equal to

$$\frac{1}{2}\dot{\varphi}^2 - \tilde{V}. \quad (85)$$

Its solutions thus correspond to periodic oscillations around local minima of the potential (Arnold, 1992). Here, we are concerned with oscillations around $\varphi = 0$. In view of the boundary conditions we are considering, any solution admits a first time ξ_c such that $\varphi'(\xi_c) = 0$. The solutions have periodicity $2\xi_c$ and, setting $C = -\tilde{V}(\varphi(\xi_c))$, we have

$$\xi_c = \sqrt{\frac{1}{2}} \int_0^{\varphi(\xi_c)} \frac{1}{\sqrt{C + \tilde{V}(\phi)}} d\phi. \quad (86)$$

The solutions are periodic successions of monotonous parts $\varphi(\xi)$, whose inverses are of the form

$$\xi(\varphi) = \xi_0 \pm \sqrt{\frac{1}{2}} \int_{\varphi(\xi_0)}^{\varphi} \frac{1}{\sqrt{C + \tilde{V}(\phi)}} d\phi. \quad (87)$$

Remark that, owing to the existence of a prime integral and because of the conditions $\varphi(0) = 0$ and $\varphi'(\xi_c) = 0$, fixing C is equivalent to fixing $\varphi'(0)$ and $\varphi(\xi_c)$. Remark also that the expressions in (86) and (87) cannot be made explicit without invoking elliptic integrals. Therefore, we shall compute by means of a numerical procedure the values of C which ensure that boundary conditions are satisfied.

At this point, we shall recap how, once fixed Λ , the current shape of the homogenized duoskelion beam model or, equivalently, the placement function χ can be retrieved. Recall that, in the reference configuration, the continuum is straight and directed along the direction \mathbf{e}_x and that the condition $\chi(0) = \mathbf{0}$ is prescribed. Once boundary conditions on φ are specified, the following steps should be undertaken to retrieve the placement function χ :

1. to solve Eq. (67) together with boundary conditions on φ ;
2. to compute the field ϑ from Eq. (59), namely

$$\tan(\varphi - \vartheta) = \Lambda \sin \varphi; \quad (88)$$

3. to compute the field ρ using the following expression

$$\begin{aligned} \rho &\stackrel{\text{Eq. (39)}}{=} \sqrt{\frac{\sin^2(\varphi - \vartheta) + \cos^2(\varphi - \vartheta)}{\cos^2(\varphi - \vartheta)}} \\ &= \sqrt{\tan^2(\varphi - \vartheta) + 1} \stackrel{\text{Eq. (59)}}{=} \sqrt{\Lambda^2 \sin^2 \varphi + 1}; \end{aligned} \quad (89)$$

4. to compute $\chi(\xi) = \chi(0) + \int_0^\xi \chi'(s) ds \stackrel{\chi(0)=0}{=} \int_0^\xi \rho(x) \mathbf{e}_{\vartheta(x)} dx$, where $\mathbf{e}_{\vartheta(x)} = \cos \vartheta(x) \mathbf{e}_x + \sin \vartheta(x) \mathbf{e}_y$, cfr. (21).

5. Computation of equilibria via Weierstrass's closed-form solution

Before presenting the results of the numerical study, some preliminary considerations based on the qualitative study of equilibrium equations discussed above will be presented. The values of the quantities Λ , L/L_0 , and \tilde{K} utilized to obtain the numerical results shown in the sequel are reported in Table 2.

5.1. Preliminary considerations

Remark that the potential $-\tilde{V}$ is an even function and it is periodic with period 2π . By means of elementary calculus, we can study the maxima and minima of the function $-\tilde{V}$ of φ for a given Λ . The results of such a study are reported in Table 3. It is worth to remark that the

Table 2

Numerical values of the quantities Λ , L/L_0 , and \tilde{K} which have been utilized to obtain the results presented in this work. All the quantities are non-dimensional.

Λ (1)		L/L_0 (1)		\tilde{K} (1)
-5	5	1	2	1

local maxima and minima of the function $-\tilde{V}$, which correspond to equilibrium points of the dynamical system (84), are nothing but the uniform solutions discussed in the previous section.

In Fig. 4, the plot of the potential $-\tilde{V}$ as a function of the angle φ is shown for four values of the load Λ , each belonging to one of the intervals in Table 3.

We remark that the angle $\varphi = 0$ is a local minimum for $-\tilde{V}$ if and only if $-1 < \Lambda < 0$ and $\|\Lambda\| \geq 1$. Therefore, only for values of the load Λ belonging to these intervals we can aim at finding solutions $\varphi(\xi)$ oscillating around the value $\varphi = 0$. To study such a kind of solutions it is necessary to subdivide the abscissa into different intervals, so that in each of these intervals the function $\xi(\varphi)$ in (87) can be inverted. Owing to the regularity of \tilde{V} , each of these intervals is separated by a value of the reference abscissa such that $\varphi' = 0$.

Fig. 5 reports for three values of Λ belonging to the intervals $-1 < \Lambda < 0$ and $\|\Lambda\| \geq 1$ the minimum value ξ_c of the reference abscissa for which $\varphi' = 0$ holds as a function of the constant C . Let $\bar{\varphi}$ be a local maximum for $-\tilde{V}$. Clearly, we have that ξ_c is an increasing function of C and that $\xi_c \rightarrow \infty$ when the constant C approaches $-\tilde{V}(\bar{\varphi})$. Indeed, because of the uniqueness of the solution to the initial value problem (84), it is not possible that in a region of the beam of finite length ξ_c the angle φ reaches $\bar{\varphi}$ with $\varphi' = 0$, because this would mean that such a trajectory intersects that corresponding to the uniform solution $\varphi = \bar{\varphi}$. Remark also that, if $C > -\tilde{V}(\bar{\varphi})$, then there does not exist a first time ξ_c such that the condition $\varphi'(\xi_c) = 0$ holds true while, if $C < -\tilde{V}(0)$, then there does not exist any solution to the initial value problem (84).

We shall now briefly explain in more detail how we construct oscillatory solutions $\varphi(\xi)$. Let us consider the condition $\varphi(L/L_0) = 0$. The condition $\varphi'(L/L_0) = 0$ can then be dealt with in a straightforward manner. At first let us note that the function $\tilde{V}(\varphi)$ is even. Let us denote with n the number of times the solution φ must intersect the value $\varphi = 0$. At this point, we seek to find the value of the constant C such that $\xi_c(C)$ is equal to $(L/L_0)/(2n - 2)$. We denote with the symbol C^* such a specific value of the constant C . We then compute numerically the integral function $\xi(\varphi)$ in (87), setting $C = C^*$, which is clearly a non-decreasing function — it can hence be inverted — in its definition interval $[0, \varphi^*]$, with $\varphi^* = \varphi(\xi_c)$. Subsequently, we compute its inverse $\varphi(\xi)$. Starting from the so-found function $\varphi(\xi)$ for the interval $\xi \in [0, \xi_c(C^*)]$, exploiting the evenness of the potential and the fact that the solution to the dynamical system (84), upon reaching $\pm\varphi^*$, passes through the same trajectory computed previously — but in the opposite direction — we construct the sought solution through successive reflections of the solution computed in the interval $\xi \in [0, \xi_c(C^*)]$ with respect to the vertical and horizontal axes.

It is worth to note that it is challenging to compute numerically the quantity ξ_c when the integrand function in (86) blows up, namely when $C = -\tilde{V}(\varphi)$. More particularly, the function $NIntegrate$ of the software Wolfram Mathematica 10,⁴ which has been used to construct the plots in Fig. 5, could not converge when $\varphi(\xi_c)$ is close to zero, i.e. $C \approx -\tilde{V}(0)$, and when $\varphi(\xi_c)$ approaches $\tilde{V}(\bar{\varphi})$, i.e. $C \approx -\tilde{V}(\bar{\varphi})$, cfr. Fig. 5.

In this regard, let us now prove that it is possible to extend by continuity the function $\xi_c(C)$ by setting $\xi_c(-\tilde{V}(0)) = \lim_{C \rightarrow -\tilde{V}(0)} \xi_c(C)$.

⁴ A global adaptive strategy has been used, which reaches the required precision and accuracy goals of the integral estimate by recursive bisection of the subregion with the largest error estimate into two halves, and computes integral and error estimates for each half

Table 3
Classification of the extreme points of the function $-\tilde{V}$ of φ .

Λ	$\varphi = -\pi$	$\varphi = -\arccos(1/\Lambda)$	$\varphi = 0$	$\varphi = \arccos(1/\Lambda)$	$\varphi = \pi$
$-1 < \Lambda < 0$	max	-	min	-	max
$0 < \Lambda < 1$	min	-	max	-	min
$\ \Lambda\ \geq 1$	min	max	min	max	min

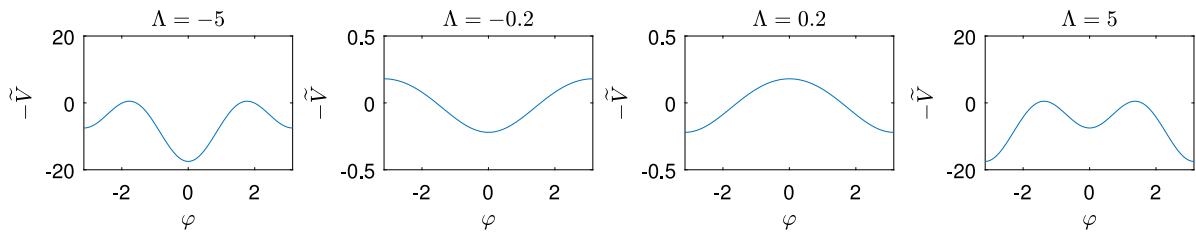


Fig. 4. Plots of the potential $-\tilde{V}$ as a function of the angle φ for four values of the load Λ , each belonging to one of the intervals in [Table 3](#). Since the potential $-\tilde{V}$ is a 2π -periodic function, we show only its plot in the interval $\varphi \in [-\pi, \pi]$.

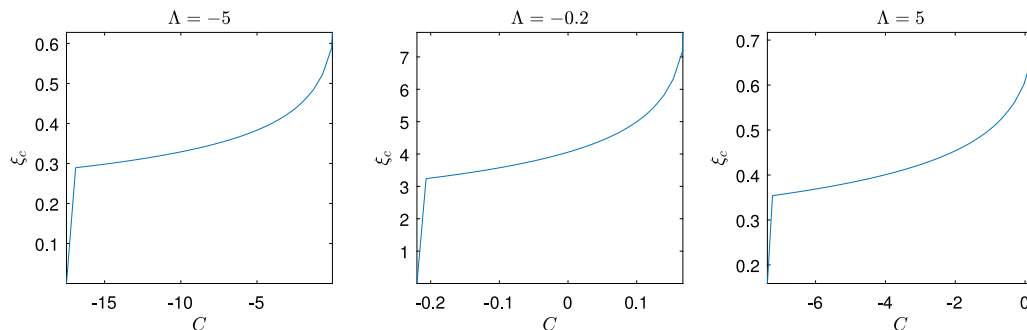


Fig. 5. Minimum value ξ_c of the reference abscissa for which $\varphi' = 0$ holds as a function of the constant C for three values of Λ belonging to the intervals $-1 < \Lambda < 0$ and $\|\Lambda\| \geq 1$ computed through the function *NIntegrate* of the software Wolfram Mathematica 10. It is seen that $\xi_c \rightarrow \infty$ when the constant C approaches $-\tilde{V}(\bar{\varphi})$. The numerical integration fails when $\varphi(\xi_c)$ is close to zero and when $\varphi(\xi_c)$ approaches $\tilde{V}(\bar{\varphi})$.

We thus consider the case where $\tilde{V}(0) + C$ is small. Clearly, the value of φ over the motion of the equivalent dynamical system is in that case bounded by the value φ_c . We note that if $\tilde{V}(0) + C$ is small in magnitude, then, considering the continuity of $\tilde{V}(\varphi)$, also φ_c must be small in magnitude. Therefore, we can satisfactorily approximate $\tilde{V}(\varphi) + C$ through a truncated second-order Taylor expansion as

$$\tilde{V}(\varphi) + C \approx \tilde{V}(0) + C + \frac{1}{2} [\tilde{V}''(0)] \varphi^2. \quad (90)$$

It is thus possible to conclude that the condition $\tilde{V}(\varphi_c) + C = 0$, namely the definition of the quantity φ_c , implies that $\tilde{V}(0) + C + \frac{1}{2} [\tilde{V}''(0)] \varphi_c^2 = 0$, which in turn implies that

$$\varphi_c = \sqrt{-\frac{2}{\tilde{V}''(0)} [\tilde{V}(0) + C]}. \quad (91)$$

Plugging the expression for φ_c in [\(86\)](#), we obtain

$$\xi_c = \sqrt{\frac{1}{2}} \int_0^{\sqrt{-\frac{2}{\tilde{V}''(0)} (\tilde{V}(0)+C)}} \frac{1}{\sqrt{\tilde{V}(0) + C + \frac{1}{2} [\tilde{V}''(0)] \varphi^2}} d\varphi. \quad (92)$$

Defining the new variable $p = \frac{\varphi}{\sqrt{-\frac{2}{\tilde{V}''(0)} (\tilde{V}(0)+C)}}$, the previous integral can be rewritten more simply as

$$\xi_c = \sqrt{-\frac{1}{\tilde{V}''(0)}} \int_0^1 \frac{1}{\sqrt{1-p^2}} dp, \quad (93)$$

which means that for $C \approx -\tilde{V}(0)$ the function $\xi_c(C)$ behaves like the constant function, as there is no dependence upon the quantity C of the right-hand side of [\(93\)](#). Note that, therefore, the function $\xi_c(C) : (-\tilde{V}(0), -\tilde{V}(\bar{\varphi})) \rightarrow \mathbb{R}^+$ admits a lower bound which is strictly

greater than zero, meaning that, if the beam is too short, non-uniform solutions may not exist.

Let us now study the asymptotic behavior of the function $\xi_c(C)$ in [\(86\)](#) when φ_c is close to $\bar{\varphi}$, a local maximum of the function $-\tilde{V}(\varphi)$. To this end, let us introduce an angle φ_0 such that $\varphi_0 < \bar{\varphi}$ and define $\bar{C} = -\tilde{V}(\bar{\varphi})$. We then write ξ_c in [\(86\)](#) as

$$\xi_c = \sqrt{\frac{1}{2}} \int_0^{\varphi_0} \frac{1}{\sqrt{C + \tilde{V}(\varphi)}} d\varphi + \sqrt{\frac{1}{2}} \int_{\varphi_0}^{\varphi_c} \frac{1}{\sqrt{C + \tilde{V}(\varphi)}} d\varphi. \quad (94)$$

Setting

$$\xi_0 = \sqrt{\frac{1}{2}} \int_0^{\varphi_0} \frac{1}{\sqrt{C + \tilde{V}(\varphi)}} d\varphi \quad (95)$$

we can rewrite ξ_c in [\(94\)](#) as

$$\xi_c = \xi_0 + \sqrt{\frac{1}{2}} \int_{\varphi_0}^{\varphi_c} \frac{1}{\sqrt{C + \tilde{V}(\varphi)}} d\varphi. \quad (96)$$

Assuming $C \approx \bar{C}$, we can satisfactorily approximate $C + \tilde{V}(\varphi)$ through a truncated second order Taylor expansion as

$$C + \tilde{V}(\varphi) \approx C - \bar{C} + \frac{1}{2} \tilde{V}''(\bar{\varphi})(\varphi - \bar{\varphi})^2. \quad (97)$$

Plugging the previous expression in [\(96\)](#), we get

$$\xi_c = \xi_0 + \frac{1}{\sqrt{\frac{1}{2} \tilde{V}''(\bar{\varphi})}} \sqrt{\frac{1}{2}} \int_{\varphi_0}^{\varphi_c} \frac{1}{\sqrt{\frac{C - \bar{C}}{\frac{1}{2} \tilde{V}''(\bar{\varphi})} + (\varphi - \bar{\varphi})^2}} d\varphi \quad (98)$$

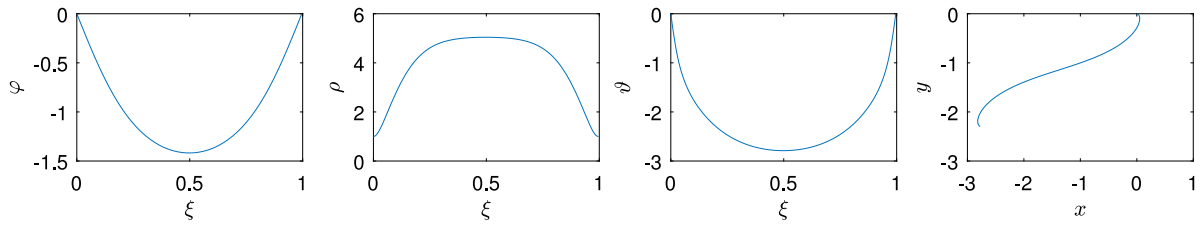


Fig. 6. Fields $\varphi(\xi)$ (left), $\rho(\xi)$ (mid-left), and $\vartheta(\xi)$ (mid-right) along with deformed equilibrium shape (right) for $L/L_0 = 1$, $\Lambda = -5$, $n = 2$, $\varphi(\xi = 0) = \varphi(\xi = 1) = 0$.

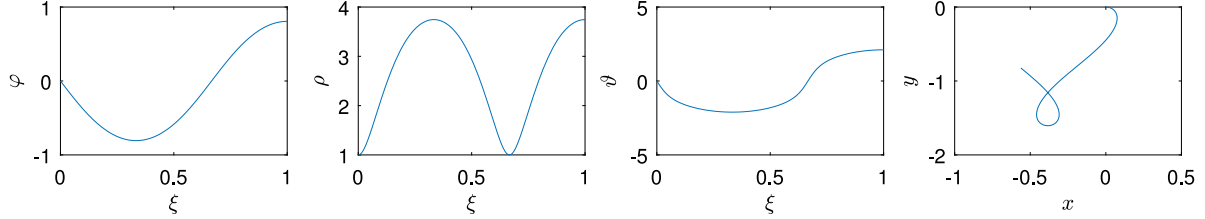


Fig. 7. Fields $\varphi(\xi)$ (left), $\rho(\xi)$ (mid-left), and $\vartheta(\xi)$ (mid-right) along with deformed equilibrium shape (right) for $L/L_0 = 1$, $\Lambda = -5$, $n = 2$, and $\varphi(\xi = 0) = 0$.

which, applying again (97),⁵ and after some elementary algebraic manipulations, reads as

$$\xi_c = \xi_0 + \frac{1}{\sqrt{(\varphi_c - \bar{\varphi})^2 \tilde{V}''(\bar{\varphi})}} \int_{\varphi_0}^{\varphi_c} \frac{1}{\sqrt{\left(\frac{\varphi - \bar{\varphi}}{\varphi_c - \bar{\varphi}}\right)^2 - 1}} d\varphi. \quad (99)$$

Defining the new variable $p = \frac{\varphi - \bar{\varphi}}{\varphi_c - \bar{\varphi}}$, we get

$$\xi_c = \xi_0 + \frac{1}{\sqrt{\tilde{V}''(\bar{\varphi})}} \int_{\frac{\varphi_0 - \bar{\varphi}}{\varphi_c - \bar{\varphi}}}^1 \frac{1}{\sqrt{p^2 - 1}} dp = \xi_0 - \frac{\cosh^{-1}\left(\frac{\varphi_0 - \bar{\varphi}}{\varphi_c - \bar{\varphi}}\right)}{\sqrt{\tilde{V}''(\bar{\varphi})}}. \quad (100)$$

Observing that $\frac{\varphi_0 - \bar{\varphi}}{\varphi_c - \bar{\varphi}} > 1$, the previous expression can be recast into the following one

$$\xi_c = \xi_0 - \frac{\log\left[\frac{\varphi_0 - \bar{\varphi}}{\varphi_c - \bar{\varphi}} + \sqrt{\left(\frac{\varphi_0 - \bar{\varphi}}{\varphi_c - \bar{\varphi}}\right)^2 - 1}\right]}{\sqrt{\tilde{V}''(\bar{\varphi})}}. \quad (101)$$

Reminding that if $C \rightarrow C_M$ then $\varphi_c \rightarrow \bar{\varphi}$, we obtain from (101) the expression

$$\xi_c = \xi_0 - \frac{1}{\sqrt{\tilde{V}''(\bar{\varphi})}} \left\{ \log[2(\varphi_0 - \bar{\varphi})] - \log(\varphi_c - \bar{\varphi}) \right\}. \quad (102)$$

Reminding that, owing to (97), we have

$$\varphi_c = \bar{\varphi} + \sqrt{\frac{2(\bar{C} - C)}{\tilde{V}''(\bar{\varphi})}}, \quad (103)$$

which yields

$$\xi_c = \left\{ \xi_0 - \frac{\log[2(\varphi_0 - \bar{\varphi})]}{\sqrt{\tilde{V}''(\bar{\varphi})}} \right\} + \frac{\log\left[\frac{2(\bar{C} - C)}{\tilde{V}''(\bar{\varphi})}\right]}{2\sqrt{\tilde{V}''(\bar{\varphi})}}. \quad (104)$$

This means that, when $C \rightarrow \bar{C}$, the function $\xi_c(C)$ diverges logarithmically.

⁵ Note that, when φ in (97) is equal to φ_c , we have

$$0 = \tilde{V}(\varphi_c) + C \approx C - \bar{C} + \frac{1}{2} \tilde{V}''(\bar{\varphi})(\varphi_c - \bar{\varphi})^2.$$

In the next two subsections, we report numerical solutions obtained when the load Λ is assumed to take negative and positive values, respectively. Recall that the conditions $\varphi(\xi = 0) = 0$ and $\chi(\xi = 0) = 0$, i.e. clamp conditions, are always prescribed on the left end of the beam. Additionally, note that, if $\varphi(\xi)$ is a solution to either problem (82) or (83), then also $-\varphi(\xi)$ is a solution to problem (82) or (83), respectively. Remark also that the solution $-\varphi(\xi)$ corresponds to reflecting the current shape $\chi([0, L/L_0])$ with respect to the horizontal axis, i.e. it corresponds to the symmetric deformed configuration. In the sequel, we will refer to *double roller* condition as the boundary condition where φ is fixed to zero, while the displacement is free, and we will refer to *free* condition as the boundary condition where neither φ nor displacement are fixed.

5.2. Compression tests

In this subsection, we report numerical solutions obtained when the load Λ is assumed to take negative values.

Clamped-double roller conditions

In the first compression test, we set the length, the loading, the essential boundary conditions on φ , and the quantity n , as follows

$$L/L_0 = 1, \quad \Lambda = -5, \quad n = 2, \quad \varphi(\xi = 0) = \varphi(\xi = 1) = 0. \quad (105)$$

By making use of the plot in Fig. 5 corresponding to $\Lambda = -5$, it is seen that to obtain a solution such that $\varphi(\xi = 0) = \varphi(\xi = 1) = 0$ and $n = 2$, i.e. which intersects two times the value $\varphi = 0$, one should set the constant C equal to $C^* = -1.05361$. For that value of C the associated angle φ^* is equal to $\varphi^* = 1.41765$ rad. The resulting solution $\varphi(\xi)$ is shown in Fig. 6, where we also report the fields $\vartheta(\xi)$ and $\rho(\xi)$, as well as the deformed equilibrium shape. It is worth to remark that extremely large displacements and rotations, as well as extremely large stretch and shear deformations, are observed. By integrating the function $\rho(\xi)$, it can be seen that the deformed equilibrium shape is almost four times longer than the initial shape while, from the deformed shape in Fig. 5, it is seen that the horizontal and vertical free end displacements are almost four times and two times greater than the initial length of the whole beam, respectively. As an instance, the center line of the middle region of the beam rotates of about π rad, and the shear angle reaches values extremely close to $-\pi/2$ rad. In Appendix B it is shown that such a solution is locally stable.

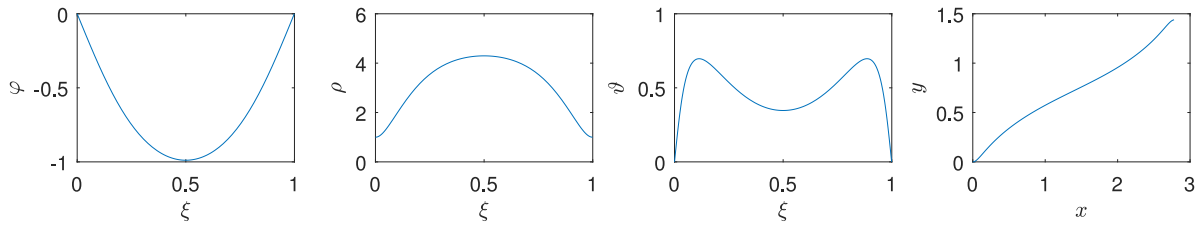


Fig. 8. Fields $\varphi(\xi)$ (left), $\rho(\xi)$ (mid-left), and $\theta(\xi)$ (mid-right) along with deformed equilibrium shape (right) for $L/L_0 = 1$, $\Lambda = 5$, $n = 2$, and $\varphi(\xi = 0) = \varphi(\xi = 1) = 0$.

Clamped-free conditions

In the second compression test, we set the length, the loading, the essential boundary conditions on φ , and the quantity n , as follows

$$L/L_0 = 1, \quad \Lambda = -5, \quad n = 2, \quad \varphi(\xi = 0) = 0. \quad (106)$$

By making use of the plot in Fig. 5 corresponding to $\Lambda = -5$, it is seen that to obtain a solution such that $\varphi(\xi = 0) = 0$ and $n = 2$, i.e. which intersects two times the value $\varphi = 0$, one should set the constant C equal to $C^* = -9.4465$. For that value of C the associated angle φ^* is equal to $\varphi^* = 0.806499$ rad. The resulting solution $\varphi(\xi)$ is shown in Fig. 7, where we also report the fields $\theta(\xi)$ and $\rho(\xi)$, as well as the deformed equilibrium shape. It is worth to remark that extremely large displacements and rotations, as well as extremely large stretch and shear deformations, are observed. Also in this case extremely large displacements, rotations, and deformations are observed. Additionally, it is worth to remark that the deformed shape of the beam forms a kind of *flake*.

5.3. Traction tests

In this subsection, we report numerical solutions obtained when the load Λ is assumed to take positive values.

Clamped-double roller conditions $L/L_0 = 1$

In the first traction test, we set the length, the loading, the essential boundary conditions on φ , and the quantity n , as follows

$$L/L_0 = 1, \quad \Lambda = 5, \quad n = 2, \quad \varphi(\xi = 0) = \varphi(\xi = 1) = 0. \quad (107)$$

By making use of the plot in Fig. 5 corresponding to $\Lambda = 5$, it is seen that to obtain a solution such that $\varphi(\xi = 0) = \varphi(\xi = 1) = 0$ and $n = 2$, i.e. which intersects two times the value $\varphi = 0$, one should set the constant C equal to $C^* = -1.02767$. For that value of C the associated angle φ^* is equal to $\varphi^* = 0.988922$ rad. The resulting solution $\varphi(\xi)$ is shown in Fig. 8, where we also report the fields $\theta(\xi)$ and $\rho(\xi)$, as well as the deformed equilibrium shape.

Clamped-double roller conditions $L/L_0 = 2$

In the second traction test, we set the length, the loading, the essential boundary conditions on φ , and the quantity n , as follows

$$L/L_0 = 2, \quad \Lambda = 5, \quad n = 3, \quad \varphi(\xi = 0) = \varphi(\xi = 2) = 0. \quad (108)$$

By making use of the plot in Fig. 5 corresponding to $\Lambda = 5$, it is seen that to obtain a solution such that $\varphi(\xi = 0) = \varphi(\xi = 2) = 0$ and $n = 3$, i.e. which intersects two times the value $\varphi = 0$, it is sufficient to exploit the result obtained for the previous traction test and, therefore, set the constant C equal to $C^* = -1.02767$. The resulting solution $\varphi(\xi)$ is shown in Fig. 9, where we also report the fields $\theta(\xi)$ and $\rho(\xi)$, as well as the deformed equilibrium shape.

6. Numerical solution of the discrete system

At the beginning, in this section, we shall resume how a discrete system with given ε can be put in relation with the homogenized

continuum system. Essentially, the discrete system is regarded as an element of a sequence of discrete systems parameterized over the generic cell size ε , whose limit for $\varepsilon \rightarrow 0$ is the continuum system. Remind that the whole duoskelion beam has a length L , which is kept unchanged in the previously-mentioned limit process $\varepsilon \rightarrow 0$. Let us consider the case $L_0 = 1$ m. Because of the definitions that have been introduced throughout the present work, the constant \tilde{K} is obtained through the relation $\tilde{K} = K/L_0^2$, while the constant K is obtained through the relationship $K = \tilde{K}_R/\tilde{K}_E$. From the latter formula we obtain

$$\tilde{K}_R = K\tilde{K}_E = \tilde{K}\tilde{K}_E L_0^2 \quad (109)$$

We remind that \tilde{K}_R is defined as (cfr. Eq. (48))

$$\tilde{K}_R = \frac{\tilde{K}_B \tilde{K}_T}{\tilde{K}_B + \tilde{K}_T}, \quad (110)$$

while the constants \tilde{K}_E , \tilde{K}_T and \tilde{K}_B are defined as (cfr. Eq. (30))

$$K_E = \tilde{K}_E \varepsilon^{-1}, \quad K_{T(B)} = \tilde{K}_{T(B)} \varepsilon^{-1}, \quad (111)$$

where the constants K_E , K_T and K_B are defined, respectively, as the stiffnesses of the extensional and top/bottom rotational springs. Combining (109) with (110) and applying the scaling, we obtain

$$\tilde{K} = \frac{1}{\tilde{K}_E L_0^2} \frac{\tilde{K}_B \tilde{K}_T}{\tilde{K}_B + \tilde{K}_T} = \frac{K_B}{2K_E L_0^2}, \quad (112)$$

where a balanced duoskelion structure has been considered. The beam is subjected to an axial force λ , which is positive in extension and negative in compression, which is linked to Λ by the relation $\Lambda = \lambda/\tilde{K}_E$. According to the considerations above, as well as to the choices $\tilde{K} = 1$ in Table 2 and $L_0 = 1$ m, it easily follows that

$$\frac{K_B}{2} = K_E \times 1 \text{ m}^2, \quad \lambda = \frac{\Lambda \times K_E}{N} \times 1 \text{ m}. \quad (113)$$

The total length of the beam considered in the numerical simulations performed with the discrete model is $L = 1$ m, i.e. $L/L_0 = 1$.

6.1. Methodology

A Timoshenko-like beam in-plane is formulated in a discrete fashion for arbitrarily large deformations (Turco et al., 2020; Turco, 2020). Such a beam consists in a finite number of consecutively connected straight links, see Fig. 10. Nodes connecting the links are numbered in such a way that adjacent nodes are labeled with two consecutive natural numbers. The current position of node j is denoted with p_j and its reference position with P_j , being $j = 1, 2, \dots, N_r$. Following the spirit of enriched continua, each node is endowed with a unit vector, that for the generic node j reads in the reference configuration as

$$\mathbf{D}_{1,j} = \frac{P_{j+1} - P_j}{\|P_{j+1} - P_j\|}. \quad (114)$$

Such a unit vector is transformed in the current configuration into the unit vector $\mathbf{d}_{1,j} = \mathbf{Q}_j \mathbf{D}_{1,j}$, being \mathbf{Q}_j a proper orthogonal second-rank rotation tensor. Therefore, reference and current configurations are determined by the sets of Lagrangian parameters $\{P_j, \mathbf{D}_{1,j}\}$ and $\{p_j, \mathbf{d}_{1,j}\}$, respectively.

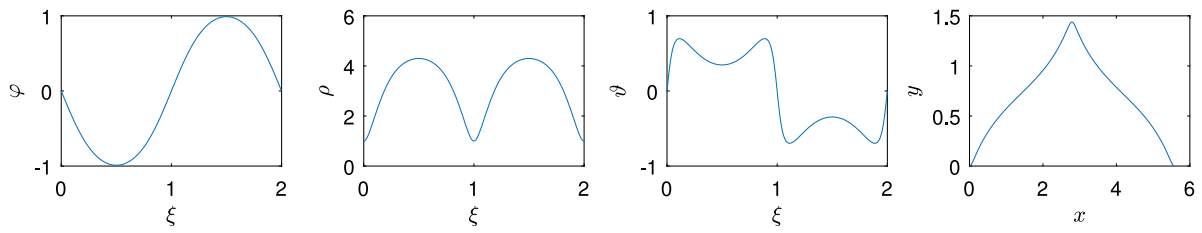


Fig. 9. Fields $\phi(\xi)$ (left), $\rho(\xi)$ (mid-left), and $\theta(\xi)$ (mid-right) along with deformed equilibrium shape (right) for $L/L_0 = 2$, $\Lambda = 5$, $n = 3$, and $\phi(\xi = 0) = \phi(\xi = 2) = 0$.

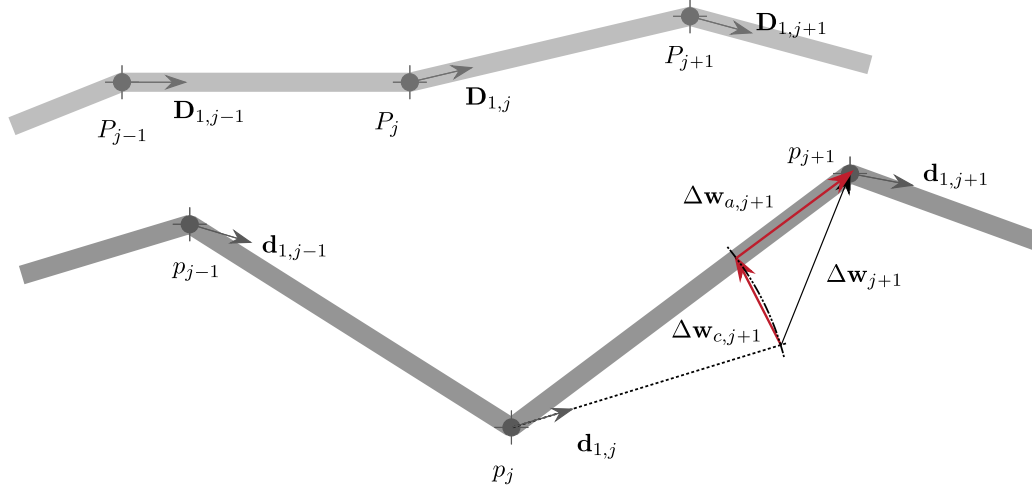


Fig. 10. Reference (light gray) and current (dark gray) configurations with related kinematic quantities. Geometrical meaning of stretch deformation $\Delta w_{a,j+1}$ and shear deformation $\Delta w_{c,j+1}$ is given in red for the generic discrete Timoshenko-like element in plane considered in this work. (For interpretation of the references to color in this figure legend, the reader is referred to the web version of this article.)

Two strain measures, i.e. Δw_{j+1} and $\Delta \mathbf{Q}_{j+1}$, are defined for the generic index j according to Fig. 10. Particularly, the vector Δw_{j+1} is given by

$$\Delta w_{j+1} = (p_{j+1} - p_j) - \|P_{j+1} - P_j\| \mathbf{Q}_j \mathbf{D}_{1,j}, \quad (115)$$

while the tensor $\Delta \mathbf{Q}_{j+1}$ is defined as

$$\Delta \mathbf{Q}_{j+1} = \mathbf{Q}_{j+1} \mathbf{Q}_j^T - \mathbf{I}, \quad (116)$$

with \mathbf{I} being the identity second-rank tensor. The strain measure $\Delta \mathbf{Q}_{j+1}$ is defined as the difference between the relative rotation tensor $\mathbf{Q}_{j+1} \mathbf{Q}_j^T$ rotating $\mathbf{d}_{1,j}$ into $\mathbf{d}_{1,j+1}$ and the identity tensor. Such a strain measure is zero only when there is no relative rotation between the j th and $j+1$ -th link, namely when the relative rotation tensor coincides with the identity. Remark that the strain measure $\Delta \mathbf{Q}_{n+1}$ is objective. Indeed, let us apply a rigid rotation \mathbf{R} to the current configuration or, equivalently, let us change the frame of reference. We obtain $\mathbf{R} \mathbf{Q}_{j+1} (\mathbf{R} \mathbf{Q}_j)^T = \mathbf{R} \mathbf{Q}_{j+1} \mathbf{Q}_j^T \mathbf{R}^T$. Hence, the relative rotation tensor appearing in the strain measure is objective. Obviously, the identity tensor is also objective. From what we have said, the strain measure $\Delta \mathbf{Q}_{n+1}$ is frame independent. The strain vector Δw_{j+1} can be additively decomposed into two terms, namely

$$\Delta w_{a,j+1} = (p_{j+1} - p_j) \left(1 - \frac{\|P_{j+1} - P_j\|}{\|p_{j+1} - p_j\|} \right), \quad (117)$$

and

$$\Delta w_{c,j+1} = \Delta w_{j+1} - \Delta w_{a,j+1}. \quad (118)$$

Each quantity in Eqs. (117) and (118) is interpreted geometrically in Fig. 10. It is easily seen that the norms of the strain measures in Eqs. (117) and (118) can be interpreted as measuring, respectively, the

stretch (link's absolute change of length) and the shear⁶ deformations of the link in-between nodes j and $j+1$. The quantity $\Delta \mathbf{Q}_j$ is a bending measure for the element formed by the two links joining, respectively, nodes $j+1/j$ and $j/j-1$. Indeed, for such an element bending is considered in the present discrete formulation as the relative rotation of $\mathbf{D}_{1,j-1}$ and $\mathbf{D}_{1,j}$, being the vectors $\mathbf{D}_{1,j-1}$ and $\mathbf{D}_{1,j}$ rotating into the vectors $\mathbf{d}_{1,j-1}$ and $\mathbf{d}_{1,j}$ in the current configuration, respectively. Such a measure of bending is defined in the present discrete formulation as the relative rotation of $\mathbf{D}_{1,j}$ and $\mathbf{D}_{1,j+1}$. It is worth remarking that the quantity $\Delta \mathbf{Q}_j + \mathbf{I} = \mathbf{Q}_j \mathbf{Q}_{j-1}^T$ is a proper orthogonal tensor. If $\mathbf{Q}_{j-1} = \mathbf{Q}_j$ then $\Delta \mathbf{Q}_j$ is the null tensor.

Relationships between the independent Lagrangian parameters used to describe the motion, i.e. displacements and rotations of nodes, and the chosen strain measures $\Delta w_{a,j}$, $\Delta w_{c,j}$ and $\Delta \mathbf{Q}_{j+1}$ have been given. We shall introduce at this point the total deformation energy of the discrete system. The total deformation energy of the discrete Timoshenko-like beam is given by the summation along the beam of three elementary contributions, namely the stretch contribution

$$E_{a,j} = \frac{k_a}{2} \|\Delta w_{a,j+1}\|^2, \quad (119)$$

the bending contribution

$$E_{b,j} = \frac{k_b}{2} \|\Delta \mathbf{Q}_{j+1}\|^2, \quad (120)$$

and the shear contribution

$$E_{c,j} = \frac{k_c}{2} \|\Delta w_{c,j+1}\|^2, \quad (121)$$

⁶ Any measure of mismatch between link's and $\mathbf{D}_{1,j}$'s directions in the current configuration is considered to be a shear deformation; remark that the shear measure illustrated in Fig. 10 is a positive increasing function of the angle formed by these two directions only when such an angle ranges from 0° to 180° , from 180° to 360° , etc

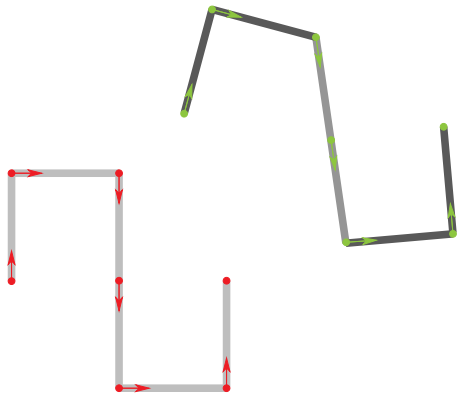


Fig. 11. Periodically repeated discretized duoskelion cell in undeformed and deformed configurations. Shear stiffness is infinite throughout the whole beam. Links which are colored in dark gray in the deformed configuration have infinite extensional stiffness. Elements formed by two adjacent links with same gray tonality in the deformed configuration have infinite bending stiffness. (For interpretation of the references to color in this figure legend, the reader is referred to the web version of this article.)

where $\|\Delta\mathbf{w}_{a,j+1}\|$ and $\|\Delta\mathbf{w}_{c,j+1}\|$ are the Euclidean norms of the vectors $\Delta\mathbf{w}_{a,j+1}$ and $\Delta\mathbf{w}_{c,j+1}$, respectively, $\|\Delta\mathbf{Q}_{j+1}\|^2 = \text{tr}(\Delta\mathbf{Q}_{j+1}^T \Delta\mathbf{Q}_{j+1})$, and k_a , k_b , and k_c are stiffness parameters⁷ corresponding to stretch, bending and shear deformations, respectively. Note that if E_a , E_b , and E_c are defined to be, respectively, the total stretching, bending, and shearing deformation energies, i.e. they are obtained by summing up, respectively, all elementary contributions in Eqs. (119), (120), and (121) along the beam, then the total deformation energy is given by $E_a + E_b + E_c$.

Remark also that, if $\mathbf{d}_{1,j}$ is required to be collinear to the link connecting nodes j and $j+1$ in the current configuration, then there is no shear deformation and one retrieves a Hencky-type discretization of the extensible Elastica which can be otherwise considered a generalization to finite deformations and extensible beams of Hencky's approximation of Euler–Bernoulli beam model. Such a generalization is discussed, e.g., in the work (Turco, 2018).

6.2. Comparison between micro- and macro- predictions

The duoskelion beam geometry shown in Fig. 1, with $N = 50$ cells, is discretized by means of the Timoshenko-like elements introduced above as shown in Fig. 11, i.e. one link for horizontal tracts and two links for vertical tracts, being the length of all links the same in the undeformed configuration. Actually, the microstructure which is studied in the present work represents a special case of such a description, as it is meant to be made by rigid two-legged bodies and purely extensible springs (see Fig. 2). Such a special case is not to be recovered by enforcing kinematic conditions — i.e. on strain measures, and hence on kinematic quantities — but rather by letting for all links the shear stiffness k_c tending to infinite.⁸ Additionally, for selected links and elements, the stretching and bending stiffnesses, respectively, tend to infinite (see the deformed configuration in Fig. 11). Links which are dark in the deformed configuration have infinite stretching stiffness. Elements formed by two adjacent links with same color in the deformed configuration have infinite bending stiffness.

Clearly, all elements and links within the system must have, strictly speaking, finite stiffnesses. Indeed, those stiffnesses which should tend to infinite are considered to be much greater than those which should

have a finite value. Numerical values for model parameters will be provided in the sequel. The discrete problem is formulated in terms of an applied force λ , and is solved by means of a modified arc-length method implemented into an in-house Matlab code, see Barchiesi et al. (2021a). Remark that, when two space dimensions are considered, the quantity $\|\Delta\mathbf{Q}_{j+1}\|^2$ in (120) is equal to $4[1 - \cos(\omega)]$, where ω is the relative rotation angle between the j th and $j+1$ -th link (Turco et al., 2020). Hence, it is different from the quantity $\sin^2(\omega)$ that one has in (1). Nevertheless, when small ω and in-plane rotations are considered, we have that $\|\Delta\mathbf{Q}_{j+1}\|^2 = 2\omega^2$ and $\sin^2(\omega) = \omega^2$. Remark also that the quantity $\|\Delta\mathbf{w}_{a,j+1}\|^2$ in (119) is the same quantity as the one $(\|p_{j+i} - p_j\| - \|P_{j+1} - P_j\|)^2$ appearing in (1). Note that, according to Fig. 11, the extensible vertical segment of a duoskelion cell is discretized with two links. Therefore, the equivalent finite extensional stiffness is equal to $k_a/2$. From the previous arguments, comparing the definitions (1), (119), and (120), it follows for the finite stiffnesses that

$$k_a = 2K_E, \quad k_b = \frac{K_B}{2}. \quad (122)$$

Therefore, for the finite stiffnesses we have that

$$k_b = k_a \times 1 \text{ m}^2, \quad \lambda = \frac{\Lambda \times k_a}{2N} \times 1 \text{ m}. \quad (123)$$

Table 4 reports the numerical values of the quantities k_a , k_b , k_c which have been utilized in computing the discrete model presented in this section. The numerical values are divided into finite ones and infinite ones, according to the discussion above. The case that we analyzed is the compression test with clamped-double roller essential conditions at boundaries. Fig. 12 shows the equilibrium path computed using the discrete model presented in this section for the compression test with clamped-double roller essential conditions at boundaries. The quantity λ in the abscissa is the absolute value of the compression force, while the quantity u_L in the ordinate is the absolute value of the horizontal (axial) displacement of the right-end tip of the duoskelion beam. It is worth to note that buckling is observed when the force reaches approximately 0.02 N and that the stiffness matrix of the discrete system is always positive definite for each converged solution step, a fact which ensures the stability of the solution computed at each converged step. Fig. 13 shows the deformed configuration of the duoskelion beam computed by means of the discrete model in the last step, corresponding to $\lambda = 0.031$ N and $u_L = 3.77$ m, compared against the deformed shape of the continuum in Fig. 6. In the discrete model, extremely large nodal displacements, as well as deformations of the deformable elements, are observed. Computations have been stopped for $\lambda = 0.031$ N, which corresponds to the value $u_L = 3.77$ m, the same computed for the continuum model. Observing that, if no information were lost in the homogenization, then, according to the expression in (123), we would have had $\lambda = 0.025$ for the considered compression test, we can conclude that the continuum approximates satisfactorily the discrete even for a relatively low number of cells. The current shape obtained with the discrete model exhibits all the main features of the one obtained by means of the continuum model. The two shapes are very similar, even if the vertical displacement of the right-end tip is noticeably different. Such a discrepancy is compatible with the fact mentioned above, namely that information is lost in the homogenization. Fig. 14 shows, on the left, the total deformation energy accumulated in the duoskelion beam and stretching, bending, and shearing energy contributions summed along the whole duoskelion beam versus the absolute value of the applied compression load. On the right, Fig. 14 shows the deformation energy accumulated in stretching, bending, and shearing energy contributions in a single duoskelion cell versus the cell number. The units of measure of all energies reported in the plots are Joules. As expected from the continuum model and compatibly with the deformed shape in Fig. 13, in the middle region of the beam most of the deformation energy is accumulated in stretching contributions, while in proximity of boundaries it is accumulated in bending contributions.

⁷ The dependence of stiffness parameters upon the index j has been omitted to lighten the notation.

⁸ In this way, the unit vector attached to each node will be co-axial to the adjacent right link.

Table 4

Numerical values of the quantities k_a , k_b , k_c which have been utilized in computing the discrete model presented in this section. The numerical values are divided into finite ones and infinite ones, according to the discussion above.

k_a (N m ⁻¹)	k_b (N m)	k_c (N m ⁻¹)	
0.5	0.5	–	fin.
1×10^5	1×10^5	1×10^5	inf.

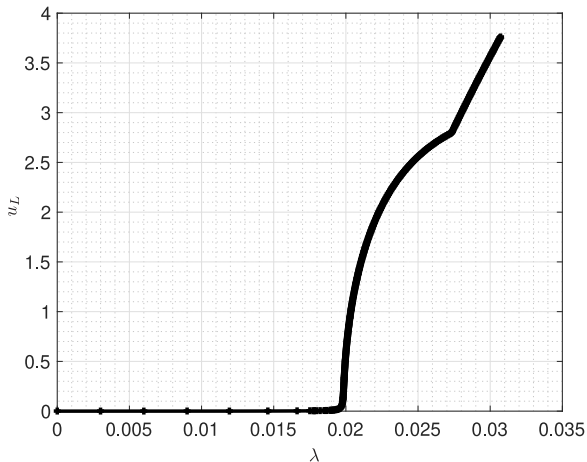


Fig. 12. Equilibrium path computed using the discrete model presented in this section for the compression test with clamped-double roller essential conditions at boundaries. The quantity λ in the abscissa is the absolute value of the compression force, while the quantity u_L in the ordinate is the absolute value of the horizontal (axial) displacement of the right end of the duoskelion beam. The units of measure of the abscissa and the ordinate are, respectively, Newton and meters. Buckling is observed when the force reaches approximately 0.02 N.

7. Conclusions and outlooks

Duoskelion structures are meant to be a proof-of-concept motif for a new class of metamaterials showing unconventional effects like axial-transverse coupling and incompressibility. In the present contribution, we have derived via asymptotic homogenization the deformation energy of a beam model describing the mechanical behavior of duoskelion structures, and then discussed and computed a class of equilibrium configurations extremely far from the reference one in the case of axial loads by exploiting the Hamiltonian structure of the equivalent dynamical system. Finally, we have shown that the homogenized model compares well with the discrete one, even when the number of cells is relatively low.

The homogenized beam model derived in this paper can be classified as an internally-constrained Cosserat (Chróscielewski et al., 2020) one-dimensional planar continuum. We shall delve more in this classification. Let us look at the deformation energy (47). For the Piola’s ansatz, we can straightforwardly interpret the quantity $\varphi(x)$ as the rotation angle of the rigid S-shaped body in the elementary unit cell centered at the abscissa x . As noted after Eq. (38), the quantity Δ in (47) can be expressed in terms of the quantities ϑ and φ as $\Delta = \varphi - \vartheta$, according to the continualization of Eq. (25). In the language of continuum mechanics, the quantity Δ hence coincides with the so-called shear deformation of the 1D continuum. Given the kinematics, i.e. placement and (cross-section-like) rotation angle fields, and the deformation energy (47), considering that for small shear angles $\tan^2 \Delta \approx \Delta^2$, it can be concluded that the homogenized model corresponds to one of the possible non-linear generalizations of the classical Timoshenko beam model. Clearly, as the constraint $\rho \cos \Delta = 1$ (see Eq. (38)) must hold almost everywhere, the homogenized model can be more specifically categorized as an internally constrained Timoshenko beam model, this last being a Cosserat-type continuum. At this point, it is

also worth to note that the (only) final governing differential equation, i.e. Eq. (67), involves only one unknown, that is a kinematic parameter representative of the microstructure. Indeed, Eq. (67) involves only one unknown, which is the rotation angle field. Such a field is the micromorphic variable of the continuum, i.e. it is directly related to the microstructure. Eq. (67) does not involve ϑ , which — contrarily to φ — is instead directly related to the centerline. Obtaining Eq. (67) has been possible because, thanks to the internal constraint, we were able, considering the case of an axially loaded duoskelion beam, to manipulate the Euler-Lagrange equilibrium equation for the variable ϑ in order to express $\tan \Delta$ as a function of φ only (see Eq. (59)).

At this point, we shall now indulge in some considerations on the employed homogenization approach. At first, we remark that the homogenization approach employed in this paper possesses the main features of asymptotic homogenization. Indeed, in our analysis we expand the independent kinematic quantities $\chi(\cdot)$ and $\varphi(\cdot)$ in powers of a small parameter (see Eq. (24), i.e. the quantity ε). Such an expansion, up to the remainder $o(\varepsilon)$, is stopped at the first order in the small parameter ε . While this could seem a limitation in catching the microstructure-induced effects, this choice has been done simply because the sought limit continuum — which we have proved to be sufficiently descriptive of the discrete structure — is not of second gradient type (with the wording *second gradient type* we refer to the appearance in the deformation energy density of the second gradient of the independent kinematic descriptors χ and/or φ), but rather of first gradient — actually micromorphic — type. Considering that the absence of second gradient terms in the Taylor expansion of the independent kinematic quantities (except what is left in the remainder $o(\varepsilon)$) above is not a limitation and that, in any case, asymptotic homogenization does not restrict to cases where the limit continuum is of second gradient type, we do not see anything against identifying our approach as *asymptotic homogenization*.

It is nevertheless worth to mention that, as it is well-known, constraining the kinematics of a micromorphic (e.g. Cosserat or, particularly, Timoshenko) one-dimensional model in a suitable way (typically when $\varphi = \vartheta'$), one can transition from a first-gradient micromorphic theory to a second gradient one. Therefore, while we have recovered in the limit a micromorphic continuum, it is not excluded that in some circumstances such a continuum could reduce to a second gradient theory.

Making use of a variational view-point (which is considered as classic nowadays in asymptotic homogenization, owing to the many celebrated contributions making use of the notion of Gamma-convergence (Padilla-Garza, 2022; Friesecke et al., 2006)), the heuristic procedure that we have employed has led us to obtain the continuum limit by letting $\varepsilon \rightarrow 0$ in the discrete deformation energy, reminding that the summation turns into an integral according to $\sum_i f(x_i) \varepsilon \xrightarrow{\varepsilon \rightarrow 0} \int_0^L f \, dx$, where f is a real valued function defined on $[0, L]$. This is the reason why only the first order in ε inside the summation — right before performing the limit — is retained as a finite quantity for ε tending to zero. Higher (than first) order terms are vanishing, while lower (than first) order ones, if any, are blowing up. There are however some non-trivial factors which determine the order of a term.

At first, we shall mention the scaling laws assumed to hold asymptotically for the micro-scale stiffnesses. In our case, we have performed a specific choice for the stiffnesses $K_{T(B),i}$, which allows to retain in the limit a finite term containing the first gradient of φ .

The assumption $r_i = o(\varepsilon^0)$ is also a key point of the homogenization process. Indeed, such a condition makes finite — and, specifically, vanishing — the terms that, after the scaling, would otherwise explode. Such an assumption is equivalent to state that the model we are interested to recover in the homogenized limit describes only continuum systems with finite energy.

Concerning the fact that the Taylor expansions of the independent kinematic quantities $\chi(\cdot)$ and $\varphi(\cdot)$ were stopped, up to the remainder, at first order in ε , we can at this point observe that, even expanding

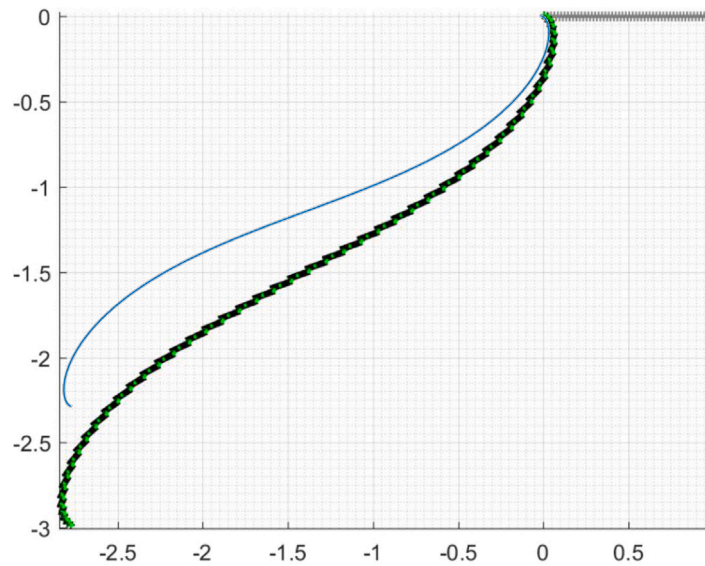


Fig. 13. Deformed configuration of the duoskelion beam computed by means of the discrete model presented in this section in the last step, corresponding to $\lambda = 0.031$ N and $u_L = 3.77$ m, compared against the deformed shape of the continuum in Fig. 6. The units of measure of the horizontal and vertical axes are meters.

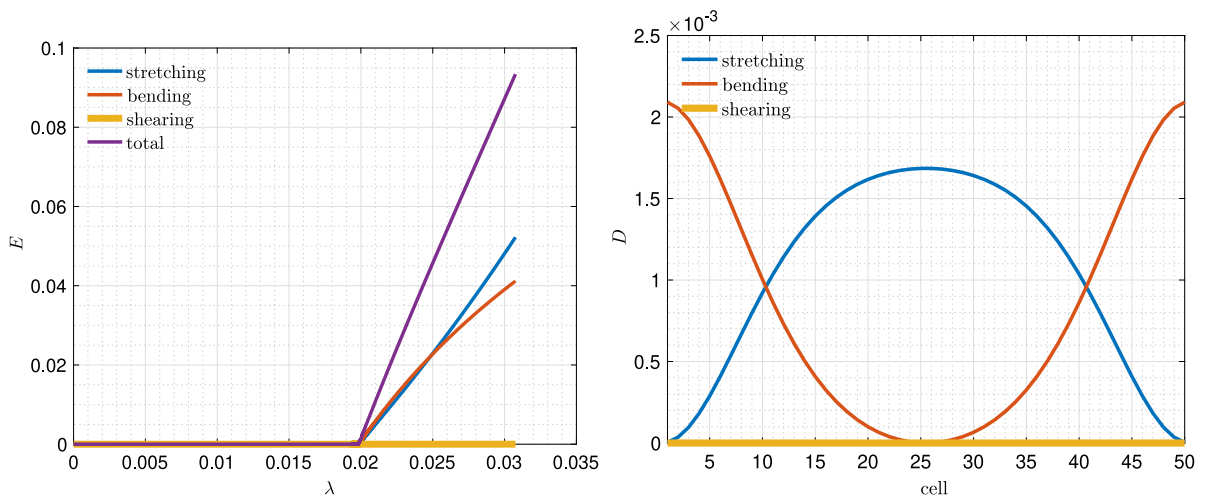


Fig. 14. On the left, total deformation energy accumulated in the duoskelion beam and stretching, bending, and shearing energy contributions summed along the whole duoskelion beam versus the absolute value of the applied compression load. On the right, deformation energy accumulated in stretching, bending, and shearing energy contributions in a single duoskelion cell versus the cell number. The units of measure of all energies reported in the plots are Joules.

the kinematic descriptors φ_i and p_i up to the second order in ε , given the dependence of the deformation energy of the discrete system upon φ_i and p_i , given the assumption $r_i = o(\varepsilon^0)$, and given the scaling laws for the micro-scale stiffnesses, the terms of the deformation energy containing higher derivatives of φ and χ would be anyway vanishing in the limit. In other words making explicit $o(\varepsilon)$ terms in the expansion of the kinematic quantities does not bring any different result, because these terms would anyway go into $o(\varepsilon)$ terms in the final — i.e. right before the limit — discrete energy expression.

We anticipate that, in a forthcoming paper, we prove a rigorous Gamma-convergence result generalizing the one which has been obtained heuristically in the present paper, and which will make clearer some points concerning the asymptotic homogenization of duoskelion structures.

It is worth to mention that, even if not addressed in the present paper and almost straightforward to see, the substitution of the S-shaped rigid bodies with any otherwise shaped rigid body does not change at all the homogenization procedure and gives the very same results.

We remark that, if one were to perform a fully discrete analysis of the duoskelion with different unit cell's aspect ratios, he/she would observe a dependence of the response, and particularly the extent of the extensional-shear coupling under axial loading, on the unit cell's aspect ratio. Apparently, this is in contradiction with one of the results that we obtained in this paper, namely the fact that the continuum-level response of the investigated metamaterial is unaffected by the unit cell's ratio. Indeed, relying on the fact that the quantity $\tan \Delta(x_i) + 2h$ — where h is the unit cell's aspect ratio — stands for the current signed length of the extensional spring on the left of node i , normalized with respect to the cell length ε (see Eq. (42)), we carried out the following argument. Since in the reference configuration the equality $\Delta = 0$ holds true, the quantity $\tan \Delta + 2h$ is greater than zero in that configuration. To pass from a positive value of such a signed length to a negative one, one must pass through a completely compressed configuration where $\tan \Delta + 2h = 0$. Such a configuration is pathological, because the continuum energy density blows up to infinity when $\tan \Delta + 2h \rightarrow 0$ (see Eq. (37)). Therefore, we have believed reasonable to limit ourselves to study only cases where $\tan \Delta + 2h \geq 0$. Under this restriction, we have proved that the homogenized response — i.e. when the number of unit

cells blows up to infinity — is unaffected by the unit cell’s aspect ratio h . It is thus possible to conclude that, while for duoskelion structures consisting of only a few unit cells the extent of the extensional-shear coupling under axial loading depends significantly on the unit cell’s aspect ratio, increasing the number of unit cells such a dependence becomes less significant until, eventually, vanishing for infinite cells, i.e. in the continuum limit.

Future outlooks of the present work include

1. performing the asymptotic homogenization adding concentrated masses to the centers of the S-shaped rigid bodies or distributed masses along such rigid bodies to deal with the dynamic regime and, more specifically, with wave propagation in duoskelion structures. This can be easily achieved following the same steps done in [Barchiesi and Khakalo \(2019\)](#), leading to rotational micro-inertia effects in the kinetic energy;
2. studying non-axial end loads by means of the same Extended Lagrangian formulation employed in this work;
3. further comparing the discrete model and the macro-model numerically — both in statics and dynamics — to assess to what extent the continuum retains the salient features of the discrete model depending on the cell size. Possible developments include the comparison of force–displacement diagrams and the computation of the discrete-continuum deformation energy error for different applied loads/displacements and cell numbers. Models more sophisticated than the discrete ones utilized in this paper could be explored at the micro-scale, as an instance semi-discrete models based on continuum beam theories ([Greco et al., 2021](#); [Greco and Cuomo, 2015, 2014](#); [Cazzani et al., 2016](#); [Harsch et al., 2021](#); [Sharma and Eremeyev, 2019](#));
4. introducing external distributed forces/couples and boundary couples;
5. investigating how to physically realize duoskelion structures, with special attention to the materialization of the extensional springs. It can be conjectured that these springs, which should be realized by physical devices that are very compliant only to extension/compression in one direction, could be materialized as pantographic beams ([Barchiesi et al., 2018, 2019](#)) constrained so to have null axial relative displacement of adjacent boundary hinges. In this manner, three scales would be clearly distinguishable in the metamaterial, namely the macro-scale ($\approx L$) of the whole duoskelion beam, the meso-scale ($\approx \varepsilon$) of the single duoskelion cell, the micro-scale of each pantographic cell making up the extensional springs;
6. exploiting the homogenization performed in this work to repeat the same study for a two-dimensional fibrous material moving in plane made up of two orthogonal families of hinged (in an analogous fashion to that of pantographic fabrics ([Spagnuolo et al., 2017](#)) and bi-pantographic fabrics ([Barchiesi et al., 2021b](#))) or rigidly connected duoskelion beams. When considering the first type of connection, one could regard the resulting two-dimensional material as a pantographic material whose fibers are duoskelion structures. It worth to remark that when the rigid connection is considered, the resulting two-dimensional model could be adapted to the granular metamaterials recently studied in [Giorgio et al. \(2020\)](#), in this regard see also the works ([Nejadsadeghi and Misra, 2021, 2020](#); [Misra and Nejadsadeghi, 2019](#)).

CRediT authorship contribution statement

Emilio Barchiesi: Conceptualization, Methodology/Study design, Software, Validation, Formal analysis, Investigation, Resources, Data curation, Writing – original draft, Writing – review & editing, Visualization, Project administration. **Francesco dell’Isola:** Conceptualization, Methodology/Study design, Formal analysis, Investigation,

Resources, Writing – review & editing, Supervision, Project administration. **Pierre Seppacher:** Conceptualization, Methodology/Study design, Formal analysis, Investigation, Resources, Writing – review & editing, Visualization, Supervision. **Emilio Turco:** Conceptualization, Methodology/Study design, Software, Validation, Investigation, Resources, Writing – original draft, Writing – review & editing, Visualization.

Declaration of competing interest

The authors declare that they have no known competing financial interests or personal relationships that could have appeared to influence the work reported in this paper.

Data availability

Data will be made available on request.

Acknowledgments

Authors would like to thank Prof. Anil Misra of Kansas University and Prof. Luca Placidi of Uninettuno University for insightful discussions onto the subject of the present paper.

Appendix A. Alternative linear stability analysis of the zero solution

In this appendix we shall study the linear stability of the zero solution to problem (77) through an alternative approach to that used in the core of the paper.

The Euler–Lagrange equation for φ associated to the second order approximation of the energy in the problem (77) reads as

$$\varphi'' - \left. \frac{\partial^2 \tilde{V}}{\partial \varphi^2} \right|_{\varphi=0} \varphi = 0, \quad (124)$$

which has infinite sinusoidal solutions of the type

$$\varphi = A \sin \left(\sqrt{\left. \frac{\partial^2 \tilde{V}}{\partial \varphi^2} \right|_{\varphi=0}} x \right), \quad (125)$$

where $A \geq 0$ is constant and is the amplitude of the sinusoidal solution. Remark that, when $A > 0$, then the solution in Eq. (125) is a real one if and only if \tilde{V} is convex in a neighborhood of $\varphi = 0$. Additionally, when $A > 0$, such a solution fulfills boundary conditions $\varphi(\xi = 0) = \varphi(\xi = 1) = 0$ if and only if

$$\sqrt{\left. \frac{\partial^2 \tilde{V}}{\partial \varphi^2} \right|_{\varphi=0}} = k\pi, \quad k \in \mathbb{Z}. \quad (126)$$

At this point we can define a family of functions, parameterized over the parameter A , which fulfill the boundary conditions $\varphi(0) = \varphi(1) = 0$ and the Euler–Lagrange equation above

$$\varphi = A \sin(k\pi x), \quad k \in \mathbb{Z}. \quad (127)$$

We remind that, since $\mathcal{E}_A = 0$ for the solution $\varphi(\xi) = 0$ (remark that such a solution can be also retrieved by setting $A = 0$ in Eq. (127)), the zero solution $\varphi(\xi) = 0$ does not only make stationary the augmented energy functional appearing in problem (77), but it is also a local minimum — and hence a locally stable solution — if other solutions (i.e. fulfilling the Euler–Lagrange equation and boundary conditions) with small magnitude are associated with positive values of the energy. Being interested in studying the linear stability of the zero solution, we plug the family of functions in Eq. (127) into the second order approximation of the energy in problem (77)

$$\int_0^1 \left(\frac{1}{2} \varphi'^2 + \frac{1}{2} \left. \frac{\partial^2 \tilde{V}}{\partial \varphi^2} \right|_{\varphi=0} \varphi^2 \right) dx$$

$$= \int_0^1 \left[\frac{1}{2} k^2 \pi^2 A^2 \cos^2(k\pi x) + \frac{1}{2} \frac{\partial^2 \tilde{V}}{\partial \varphi^2} \Big|_{\varphi=0} A^2 \sin^2(k\pi x) \right] dx ,$$

which, by means of a few manipulations and the computation of an elementary integral, reads as

$$\int_0^1 \left(\frac{1}{2} \varphi'^2 + \frac{1}{2} \frac{\partial^2 \tilde{V}}{\partial \varphi^2} \Big|_{\varphi=0} \varphi^2 \right) dx = \frac{A^2}{4} \left(k^2 \pi^2 + \frac{\partial^2 \tilde{V}}{\partial \varphi^2} \Big|_{\varphi=0} \right) .$$

For $0 < A < 1$ we have $\frac{\partial^2 \tilde{V}}{\partial \varphi^2} \Big|_{\varphi=0} > 0$. Indeed, we have that

$$\frac{\partial^2 \tilde{V}}{\partial \varphi^2} \Big|_{\varphi=0} = -\frac{A}{\tilde{K}} \left(A \cos^2 \varphi - A \sin^2 \varphi - \cos \varphi \right) \Big|_{\varphi=0} = -\frac{A(A-1)}{\tilde{K}} .$$

We hence get to the same conclusions reported after Eq. (81).

Appendix B. Stability analysis of non-uniform solutions

In this appendix we shall propose an approximate way to check the local stability of any (hence also non-uniform) solution to problem (65). More specifically, we shall be interested in studying the stability of the solution computed for the compression test with clamped-double roller conditions in Section 5.

At first, the second variation of the augmented energy functional \mathfrak{E}_A in (64) can be easily computed as

$$\delta^2 \mathfrak{E}_A = \int_0^{L/L_0} \left\{ (\delta\varphi')^2 - \frac{A}{\tilde{K}} [-\cos(\varphi) + 2A(\cos^2 \varphi - \sin^2 \varphi)] (\delta\varphi)^2 \right\} d\xi . \quad (128)$$

A solution $\varphi(\xi)$ to problem (65) is locally stable if and only if $\delta^2 \mathfrak{E}_A$ in (128) is positive for any kinematically admissible variation $\delta\varphi$. At this point, we introduce a uniform discretization $\{\xi_i\}_{i=0}^{N_F-1}$ of the domain $[0, L/L_0]$ consisting of N_F knots, such that $\xi_0 = 0$. Let us approximate $\delta\varphi'$ as

$$\delta\varphi' \approx \psi' := \sum_{i=0}^{N_F-2} \alpha_i \mathbb{I}_{[\xi_i, \xi_{i+1}]} , \quad (129)$$

where $\alpha_i \in \mathbb{R}$ and \mathbb{I} is the indicator function defined as

$$\mathbb{I}_{[\xi_i, \xi_{i+1}]}(s) = \begin{cases} 1 & s \in [\xi_i, \xi_{i+1}] \\ 0 & \text{otherwise} \end{cases} . \quad (130)$$

The previous definition allows us to compute $\psi \approx \delta\varphi$ as

$$\psi(\xi) = \int_0^\xi \psi'(s) ds = \int_0^\xi \left[\sum_{i=0}^{N_F-2} \alpha_i \mathbb{I}_{[\xi_i, \xi_{i+1}]}(s) \right] ds . \quad (131)$$

Defining the quantity N_ξ as the value of the minimum index i such that $\xi_i \geq \xi$, we obtain

$$\psi(\xi) = \Delta\xi \left(\sum_{i=0}^{N_\xi-2} \alpha_i \right) + \alpha_{N_\xi-1} (\xi - \xi_{N_\xi-1}) , \quad (132)$$

where $\Delta\xi = \xi_{i+1} - \xi_i$, a quantity which does not depend on the index i .

Note that, when $\xi = 0$, we have $\psi(0) = 0$, which is in agreement with the condition $\delta\varphi(\xi = 0) = 0$. Since we are interested in studying the stability of the solution computed for the compression test with clamped-double roller conditions in Section 5, we have that the value of the field φ is assigned also at the boundary $\xi = L/L_0$, which implies that $\delta\varphi(\xi = L/L_0) = 0$. Let us hence enforce that $\psi(L/L_0) = 0$. We obtain

$$\Delta\xi \left[\left(\sum_{i=0}^{N_F-3} \alpha_i \right) + \alpha_{N_F-2} \right] = 0 , \quad (133)$$

which allows us to find a closed-form expression for α_{N_F-2}

$$\alpha_{N_F-2} = - \sum_{i=0}^{N_F-3} \alpha_i . \quad (134)$$

Plugging (134) into (129) and (132), we get

$$\psi(\xi) = \begin{cases} \Delta\xi \left(\sum_{i=0}^{N_\xi-2} \alpha_i \right) + \alpha_{N_\xi-1} (\xi - \xi_{N_\xi-1}) & \text{if } \xi < L/L_0 - \Delta\xi \\ \left(\xi_{N_F-2} + \Delta\xi - \xi \right) \sum_{i=0}^{N_F-3} \alpha_i & \text{otherwise} \end{cases} \quad (135)$$

$$\psi'(\xi) = \sum_{i=0}^{N_F-3} \alpha_i \left(\mathbb{I}_{[\xi_i, \xi_{i+1}]} - \mathbb{I}_{[\xi_{N_F-2}, \xi_{N_F-1}]} \right) \quad (136)$$

Substituting these approximations of $\delta\varphi$ and $\delta\varphi'$ into the expression (128) of the second variation of the augmented energy functional \mathfrak{E}_A in (64), we find

$$\delta^2 \mathfrak{E}_A = \int_0^{L/L_0} \left[\sum_{i=0}^{N_F-3} \alpha_i \left(\mathbb{I}_{[\xi_i, \xi_{i+1}]} - \mathbb{I}_{[\xi_{N_F-2}, \xi_{N_F-1}]} \right) \right]^2 d\xi \quad (137)$$

$$- \int_0^{L/L_0 - \Delta\xi} \frac{A}{\tilde{K}} [-\cos(\varphi) + 2A(\cos^2 \varphi - \sin^2 \varphi)] \times \left[\Delta\xi \left(\sum_{i=0}^{N_\xi-2} \alpha_i \right) + \alpha_{N_\xi-1} (\xi - \xi_{N_\xi-1}) \right]^2 d\xi \quad (138)$$

$$- \int_{L/L_0 - \Delta\xi}^{L/L_0} \frac{A}{\tilde{K}} [-\cos(\varphi) + 2A(\cos^2 \varphi - \sin^2 \varphi)] \times \left[\left(\xi_{N_F-2} + \Delta\xi - \xi \right) \sum_{i=0}^{N_F-3} \alpha_i \right]^2 d\xi \quad (139)$$

Discretizing the integral operator in the equation above using a Riemann sum, with the same space discretization $\{\xi_j\}$ introduced at the beginning of this appendix, we obtain

$$\delta^2 \mathfrak{E}_A(\{\alpha_i\}) = \sum_{j=0}^{N_F-2} \left[\sum_{i=0}^{N_F-3} \alpha_i \left(\delta_{ij} - \delta_{(N_F-2)j} \right) \right]^2 \Delta\xi \quad (140)$$

$$- \sum_{j=0}^{N_F-2} \left\{ \frac{A}{\tilde{K}} [-\cos(\varphi_j) + 2A(\cos^2(\varphi_j) - \sin^2(\varphi_j))] \times \left(\sum_{i=0}^{j-1} \alpha_i \right)^2 (\Delta\xi)^3 \right\} , \quad (141)$$

which is a (purely) quadratic non-diagonal form in α_i 's, whose Hessian can be computed as

$$\frac{\partial^2 (\delta^2 \mathfrak{E}_A)}{\partial \alpha_h \partial \alpha_k} = 2 \sum_{j=0}^{N_F-2} \left[\sum_{i=0}^{N_F-3} \delta_{ih} \left(\delta_{ij} - \delta_{(N_F-2)j} \right) \right] \times \left[\sum_{i=0}^{N_F-3} \delta_{ik} \left(\delta_{ij} - \delta_{(N_F-2)j} \right) \right] \Delta\xi \quad (142)$$

$$- 2 \sum_{j=1}^{N_F-2} \left\{ \frac{A}{\tilde{K}} (-\cos(\varphi_j) + 2A[\cos^2(\varphi_j) - \sin^2(\varphi_j)]) \times \left(\sum_{i=0}^{j-1} \delta_{ih} \right) \left(\sum_{i=0}^{j-1} \delta_{ik} \right) (\Delta\xi)^3 \right\} . \quad (143)$$

Noting that the approximations of $\delta\varphi$ and $\delta\varphi'$ in (135) and (136), respectively, are kinematically admissible for any $\{\alpha_i\}_{i=0}^{N_F-3}$, in order to prove that the solution computed for the compression test with clamped-double roller conditions in Section 5 is stable, it is sufficient to prove that the Hessian matrix above is positive definite. We checked for $\Delta\xi = 0.1$, $\Delta\xi = 0.05$, and $\Delta\xi = 0.02$ that, for the solution $\varphi(\xi)$ shown in Fig. 6, this condition is fulfilled.

References

Abali, B.E., Müller, W.H., Eremeyev, V.A., 2015. Strain gradient elasticity with geometric nonlinearities and its computational evaluation. *Mech. Adv. Mater. Modern Proc.* 1 (1), 1–11.

- Abdoul-Anziz, H., Jakabčič, L., Seppecher, P., 2021. Homogenization of an elastic material reinforced by very strong fibres arranged along a periodic lattice. *Proc. R. Soc. Lond. Ser. A Math. Phys. Eng. Sci.* 477 (2246), 20200620.
- Abdoul-Anziz, H., Seppecher, P., 2018. Strain gradient and generalized continua obtained by homogenizing frame lattices. *Math. Mech. Complex Syst.* 6 (3), 213–250.
- Abdoul-Anziz, H., Seppecher, P., Bellis, C., 2019. Homogenization of frame lattices leading to second gradient models coupling classical strain and strain-gradient terms. *Math. Mech. Solids* 24 (12), 3976–3999.
- Altenbach, J., Altenbach, H., Eremeyev, V.A., 2010. On generalized Cosserat-type theories of plates and shells: a short review and bibliography. *Arch. Appl. Mech.* 80 (1), 73–92.
- Altenbach, H., Birsan, M., Eremeyev, V.A., 2013. Cosserat-type rods. In: *Generalized Continua from the Theory to Engineering Applications*. Springer, pp. 179–248.
- Altenbach, H., Eremeyev, V.A., 2009. On the linear theory of micropolar plates. *ZAMM-J. Appl. Math. Mech./Zeitschrift FÜR Angew. Math. Und Mech.* 89 (4), 242–256.
- Arnold, V.I., 1992. *Ordinary Differential Equations*. Springer Science & Business Media.
- Barchiesi, E., dell’Isola, F., Bersani, A.M., Turco, E., 2021a. Equilibria determination of elastic articulated duoskelion beams in 2D via a Riks-type algorithm. *Int. J. Non-Linear Mech.* 128, 103628.
- Barchiesi, E., dell’Isola, F., Hild, F., 2021b. On the validation of homogenized modeling for bi-pantographic metamaterials via digital image correlation. *Int. J. Solids Struct.* 208, 49–62.
- Barchiesi, E., Eugster, S.R., dell’Isola, F., Hild, F., 2020. Large in-plane elastic deformations of bi-pantographic fabrics: asymptotic homogenization and experimental validation. *Math. Mech. Solids* 25 (3), 739–767.
- Barchiesi, E., Eugster, S.R., Placidi, L., dell’Isola, F., 2019. Pantographic beam: a complete second gradient 1D-continuum in plane. *Z. Angew. Math. Phys.* 70 (5), 1–24.
- Barchiesi, E., Khakalo, S., 2019. Variational asymptotic homogenization of beam-like square lattice structures. *Math. Mech. Solids* 24 (10), 3295–3318.
- Barchiesi, E., Laudato, M., Di Cosmo, F., 2018. Wave dispersion in non-linear pantographic beams. *Mech. Res. Commun.* 94, 128–132.
- Battista, A., Della Corte, A., Seppecher, P., et al., 2018. Large deformations of 1D microstructured systems modeled as generalized Timoshenko beams. *Z. Angew. Math. Phys.* 69 (3), 1–22.
- Cao, X., Zhang, D., Liao, B., Fang, S., Liu, L., Gao, R., Li, Y., 2020. Numerical analysis of the mechanical behavior and energy absorption of a novel P-lattice. *Thin-Walled Struct.* 157, 107147.
- Cazzani, A., Malagù, M., Turco, E., 2016. Isogeometric analysis of plane-curved beams. *Math. Mech. Solids* 21 (5), 562–577.
- Cherkaev, A., Ryvkin, M., 2019. Damage propagation in 2D beam lattices: 2. Design of an isotropic fault-tolerant lattice. *Arch. Appl. Mech.* 89 (3), 503–519.
- Chróścielewski, J., dell’Isola, F., Eremeyev, V.A., Sabik, A., 2020. On rotational instability within the nonlinear six-parameter shell theory. *Int. J. Solids Struct.* 196, 179–189.
- Coutris, N., Thompson, L.L., Kosaraju, S., 2020. Asymptotic homogenization models for pantographic lattices with variable order rotational resistance at pivots. *J. Mech. Phys. Solids* 134, 103718.
- De Angelo, M., Barchiesi, E., Giorgio, I., Abali, B.E., 2019. Numerical identification of constitutive parameters in reduced-order bi-dimensional models for pantographic structures: application to out-of-plane buckling. *Arch. Appl. Mech.* 89 (7), 1333–1358.
- De Angelo, M., Placidi, L., NejadSadeghi, N., Misra, A., 2020. Non-standard Timoshenko beam model for chiral metamaterial: Identification of stiffness parameters. *Mech. Res. Commun.* 103, 103462.
- Della Corte, A., Battista, A., Seppecher, P., et al., 2019. Large deformations of Timoshenko and Euler beams under distributed load. *Z. Angew. Math. Phys.* 70 (2), 1–19.
- dell’Isola, F., Corte, A.D., Giorgio, I., 2017. Higher-gradient continua: The legacy of Piola, Mindlin, Sedov and Toupin and some future research perspectives. *Math. Mech. Solids* 22 (4), 852–872.
- dell’Isola, F., Eugster, S.R., Fedele, R., Seppecher, P., 2022. Second-gradient continua: From Lagrangian to Eulerian and back. *Math. Mech. Solids* 10812865221078822.
- dell’Isola, F., Giorgio, I., Pawlikowski, M., Rizzi, N.L., 2016. Large deformations of planar extensible beams and pantographic lattices: heuristic homogenization, experimental and numerical examples of equilibrium. *Proc. R. Soc. A: Math. Phys. Eng. Sci.* 472 (2185), 20150790.
- dell’Isola, F., Seppecher, P., Alibert, J.J., Lekszycki, T., Grygoruk, R., Pawlikowski, M., Steigmann, D., Giorgio, I., Andraus, U., Turco, E., et al., 2019. Pantographic metamaterials: an example of mathematically driven design and of its technological challenges. *Contin. Mech. Thermodyn.* 31 (4), 851–884.
- dell’Isola, F., Seppecher, P., Madeo, A., 2012. How contact interactions may depend on the shape of Cauchy cuts in N-th gradient continua: approach “à la D’Alembert”. *Z. Angew. Math. Phys.* 63 (6), 1119–1141.
- Elishakoff, I., 2020. Who developed the so-called Timoshenko beam theory? *Math. Mech. Solids* 25 (1), 97–116.
- Eremeyev, V.A., dell’Isola, F., Boutin, C., Steigmann, D., 2018. Linear pantographic sheets: existence and uniqueness of weak solutions. *J. Elasticity* 132 (2), 175–196.
- Eremeyev, V.A., Pietraszkiewicz, W., 2012. Material symmetry group of the non-linear polar-elastic continuum. *Int. J. Solids Struct.* 49 (14), 1993–2005.
- Eremeyev, V.A., Turco, E., 2020. Enriched buckling for beam-lattice metamaterials. *Mech. Res. Commun.* 103, 103458.
- Eugster, S.R., dell’Isola, F., Fedele, R., Seppecher, P., 2022. Piola transformations in second-gradient continua. *Mech. Res. Commun.* 103836.
- Fischer, S.C., Hillen, L., Eberl, C., 2020. Mechanical metamaterials on the way from laboratory scale to industrial applications: challenges for characterization and scalability. *Materials* 13 (16), 3605.
- Friesecke, G., James, R.D., Müller, S., 2006. A hierarchy of plate models derived from nonlinear elasticity by gamma-convergence. *Arch. Ration. Mech. Anal.* 180 (2), 183–236.
- Giorgio, I., 2016. Numerical identification procedure between a micro-Cauchy model and a macro-second gradient model for planar pantographic structures. *Z. Angew. Math. Phys.* 67 (4), 1–17.
- Giorgio, I., dell’Isola, F., Misra, A., 2020. Chirality in 2D Cosserat media related to stretch-micro-rotation coupling with links to granular micromechanics. *Int. J. Solids Struct.* 202, 28–38.
- Greco, L., Cuomo, M., 2014. An implicit G1 multi patch B-spline interpolation for Kirchhoff-Love space rod. *Comput. Methods Appl. Mech. Engrg.* 269, 173–197.
- Greco, L., Cuomo, M., 2015. Consistent tangent operator for an exact Kirchhoff rod model. *Contin. Mech. Thermodyn.* 27 (4), 861–877.
- Greco, L., Scrofani, A., Cuomo, M., 2021. A non-linear symmetric G1-conforming Bézier finite element formulation for the analysis of Kirchhoff beam assemblies. *Comput. Methods Appl. Mech. Engrg.* 387, 114176.
- Harsch, J., Capobianco, G., Eugster, S.R., 2021. Finite element formulations for constrained spatial nonlinear beam theories. *Math. Mech. Solids* 26 (12), 1838–1863.
- Harsch, J., Eugster, S.R., 2020. Finite element analysis of planar nonlinear classical beam theories. In: *Developments and Novel Approaches in Nonlinear Solid Body Mechanics*. Springer, pp. 123–157.
- Heinonen, J., et al., 2001. *Lectures on Analysis on Metric Spaces*. Springer Science & Business Media.
- Jakabčič, L., Seppecher, P., 2020. On periodic homogenization of highly contrasted elastic structures. *J. Mech. Phys. Solids* 144, 104104.
- Misra, A., NejadSadeghi, N., 2019. Longitudinal and transverse elastic waves in 1D granular materials modeled as micromorphic continua. *Wave Motion* 90, 175–195.
- Misra, A., NejadSadeghi, N., De Angelo, M., Placidi, L., 2020. Chiral metamaterial predicted by granular micromechanics: verified with 1D example synthesized using additive manufacturing. *Contin. Mech. Thermodyn.* 32 (5), 1497–1513.
- NejadSadeghi, N., Misra, A., 2020. Role of higher-order inertia in modulating elastic wave dispersion in materials with granular microstructure. *Int. J. Mech. Sci.* 185, 105867.
- NejadSadeghi, N., Misra, A., 2021. On the statics and dynamics of granular-microstructured rods with higher order effects. *Math. Mech. Solids* 26 (12), 1815–1837.
- Padilla-Garza, D., 2022. Dimension reduction through gamma convergence for general prestrained thin elastic sheets. *Calc. Var. Partial Differential Equations* 61 (5), 1–40.
- Pietraszkiewicz, W., Eremeyev, V., 2009. On natural strain measures of the non-linear micropolar continuum. *Int. J. Solids Struct.* 46 (3–4), 774–787.
- Placidi, L., Andraus, U., Della Corte, A., Lekszycki, T., 2015. Gedanken experiments for the determination of two-dimensional linear second gradient elasticity coefficients. *Z. Angew. Math. Phys.* 66 (6), 3699–3725.
- Placidi, L., Andraus, U., Giorgio, I., 2017. Identification of two-dimensional pantographic structure via a linear D4 orthotropic second gradient elastic model. *J. Eng. Math.* 103 (1), 1–21.
- Placidi, L., Greco, L., Bucci, S., Turco, E., Rizzi, N.L., 2016. A second gradient formulation for a 2D fabric sheet with inextensible fibres. *Z. Angew. Math. Phys.* 67 (5), 1–24.
- Seppecher, P., Spagnuolo, M., Barchiesi, E., Hild, F., Lekszycki, T., Giorgio, I., Placidi, L., Andraus, U., Cuomo, M., Eugster, S.R., et al., 2019. Advances in pantographic structures: design, manufacturing, models, experiments and image analyses. *Contin. Mech. Thermodyn.* 31 (4).
- Sharma, B.L., Eremeyev, V.A., 2019. Wave transmission across surface interfaces in lattice structures. *Internat. J. Engrg. Sci.* 145, 103173.
- Spagnuolo, M., Barcz, K., Pfaff, A., dell’Isola, F., Franciosi, P., 2017. Qualitative pivot damage analysis in aluminum printed pantographic sheets: numerics and experiments. *Mech. Res. Commun.* 83, 47–52.
- Spagnuolo, M., Scerrato, D., 2020. The mechanical diode: on the tracks of James Maxwell employing mechanical–electrical analogies in the design of metamaterials. In: *Developments and Novel Approaches in Biomechanics and Metamaterials*. Springer, pp. 459–469.
- Turco, E., 2018. Discrete is it enough? The revival of Piola-Hencky keynotes to analyze three-dimensional Elastica. *Contin. Mech. Thermodyn.* 30 (5).
- Turco, E., 2019. How the properties of pantographic elementary lattices determine the properties of pantographic metamaterials. In: *New Achievements in Continuum Mechanics and Thermodynamics*. Springer, pp. 489–506.
- Turco, E., 2020. Modelling of two-dimensional Timoshenko beams in Hencky fashion. In: *Developments and Novel Approaches in Nonlinear Solid Body Mechanics*. Springer, pp. 159–177.

- Turco, E., Barchiesi, E., Giorgio, I., dell'Isola, F., 2020. A Lagrangian Hencky-type non-linear model suitable for metamaterials design of shearable and extensible slender deformable bodies alternative to Timoshenko theory. *Int. J. Non-Linear Mech.* 123, 103481.
- Turco, E., Golaszewski, M., Cazzani, A., Rizzi, N.L., 2016. Large deformations induced in planar pantographic sheets by loads applied on fibers: experimental validation of a discrete Lagrangian model. *Mech. Res. Commun.* 76, 51–56.
- Turco, E., Golaszewski, M., Giorgio, I., D'Annibale, F., 2017. Pantographic lattices with non-orthogonal fibres: experiments and their numerical simulations. *Composites B* 118, 1–14.
- Turco, E., Misra, A., Pawlikowski, M., dell'Isola, F., Hild, F., 2018. Enhanced Piola–Hencky discrete models for pantographic sheets with pivots without deformation energy: numerics and experiments. *Int. J. Solids Struct.* 147, 94–109.
- Vaiana, N., Capuano, R., Sessa, S., Marmo, F., Rosati, L., 2021a. Nonlinear dynamic analysis of seismically base-isolated structures by a novel open-sees hysteretic material model. *Appl. Sci.* 11 (3), 900.
- Vaiana, N., Losanno, D., Ravichandran, N., 2021b. A novel family of multiple springs models suitable for biaxial rate-independent hysteretic behavior. *Comput. Struct.* 244, 106403.
- Vangelatos, Z., Gu, G.X., Grigoropoulos, C.P., 2019a. Architected metamaterials with tailored 3D buckling mechanisms at the microscale. *Extrem. Mech. Lett.* 33, 100580.
- Vangelatos, Z., Komvopoulos, K., Grigoropoulos, C.P., 2019b. Vacancies for controlling the behavior of microstructured three-dimensional mechanical metamaterials. *Math. Mech. Solids* 24 (2), 511–524.
- Vangelatos, Z., Melissinaki, V., Farsari, M., Komvopoulos, K., Grigoropoulos, C.P., 2019c. Intertwined microlattices greatly enhance the performance of mechanical metamaterials. *Math. Mech. Solids* 24 (8), 2636–2648.
- Yang, H., Abali, B.E., Müller, W.H., Barboura, S., Li, J., 2022. Verification of asymptotic homogenization method developed for periodic architected materials in strain gradient continuum. *Int. J. Solids Struct.* 238, 111386.
- Yang, H., Abali, B.E., Timofeev, D., Müller, W.H., 2020. Determination of metamaterial parameters by means of a homogenization approach based on asymptotic analysis. *Contin. Mech. Thermodyn.* 32 (5), 1251–1270.
- Yang, H., Timofeev, D., Abali, B.E., Li, B., Müller, W.H., 2021. Verification of strain gradient elasticity computation by analytical solutions. *ZAMM-J. Appl. Math. Mech./Zeitschrift FÜR Angew. Math. Und Mech.* 101 (12), e202100023.
- Zheng, X., Lee, H., Weisgraber, T.H., Shusteff, M., DeOtte, J., Duoss, E.B., Kuntz, J.D., Biener, M.M., Ge, Q., Jackson, J.A., et al., 2014. Ultralight, ultrastiff mechanical metamaterials. *Science* 344 (6190), 1373–1377.